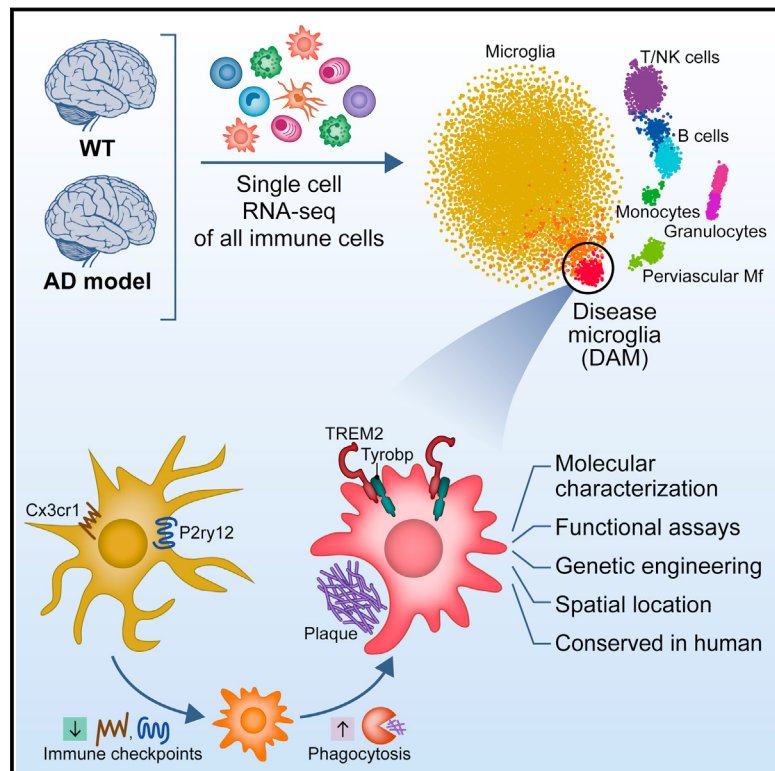


# A Unique Microglia Type Associated with Restricting Development of Alzheimer's Disease

## Graphical Abstract



## Authors

Hadas Keren-Shaul, Amit Spinrad,  
Assaf Weiner, ..., Marco Colonna,  
Michal Schwartz, Ido Amit

## Correspondence

assaf.weiner@weizmann.ac.il (A.W.),  
michal.schwartz@weizmann.ac.il (M.S.),  
ido.amit@weizmann.ac.il (I.A.)

## In Brief

A new type of microglia associated with restricting neurodegeneration may have important implications for treatment of Alzheimer's and related diseases.

37248 cells in total:  
8016 (6 WT/5XFAD mice)  
+ 1358 (5XFAD at 1, 3, 6, 8m)  
+ 6347 cells (dissected CTX, CB of WT/AD mice)  
+ 3194 (ALS mouse spinal cord)...

## Highlights

- Single-cell RNA-seq in Alzheimer's model identified a novel microglia type (DAM)
- DAM are Alzheimer's disease-associated phagocytic cells conserved in mice and human
- DAM are activated sequentially by Trem2-independent and -dependent pathways
- DAM activation requires downregulation of microglia inhibitory-checkpoint pathways

# A Unique Microglia Type Associated with Restricting Development of Alzheimer's Disease

Hadas Keren-Shaul,<sup>1,6</sup> Amit Spinrad,<sup>1,2,6</sup> Assaf Weiner,<sup>1,3,6,\*</sup> Orit Matcovitch-Natan,<sup>1,2,6</sup> Raz Dvir-Szternfeld,<sup>2</sup> Tyler K. Ulland,<sup>4</sup> Eyal David,<sup>1</sup> Kuti Baruch,<sup>2</sup> David Lara-Astaiso,<sup>1</sup> Beata Toth,<sup>5</sup> Shalev Itzkovitz,<sup>5</sup> Marco Colonna,<sup>4</sup> Michal Schwartz,<sup>2,7,\*</sup> and Ido Amit<sup>1,7,8,\*</sup>

<sup>1</sup>Department of Immunology, Weizmann Institute of Science, Rehovot 7610001, Israel

<sup>2</sup>Department of Neurobiology, Weizmann Institute of Science, Rehovot 7610001, Israel

<sup>3</sup>Hubrecht Institute-KNAW (Royal Netherlands Academy of Arts and Sciences), and University Medical Center, Cancer Genomics Netherlands, 3584 CG Utrecht, the Netherlands

<sup>4</sup>Department of Pathology and Immunology, Washington University School of Medicine, St. Louis, MO 63110, USA

<sup>5</sup>Department of Molecular Cell Biology, Weizmann Institute of Science, Rehovot 7610001, Israel

<sup>6</sup>These authors contributed equally

<sup>7</sup>Senior author

<sup>8</sup>Lead Contact

\*Correspondence: assaf.weiner@weizmann.ac.il (A.W.), michal.schwartz@weizmann.ac.il (M.S.), ido.amit@weizmann.ac.il (I.A.)

<http://dx.doi.org/10.1016/j.cell.2017.05.018>

## SUMMARY

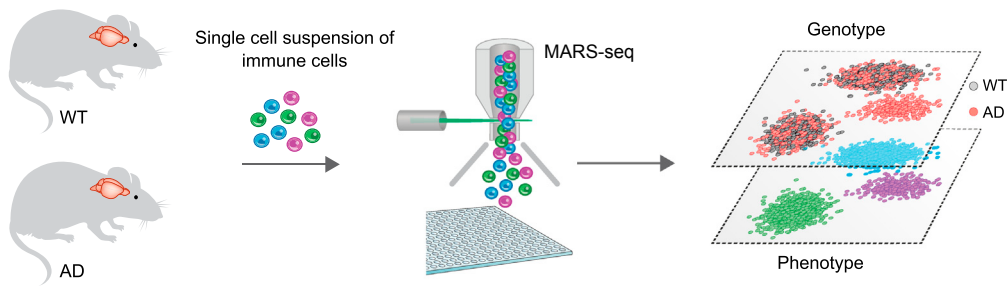
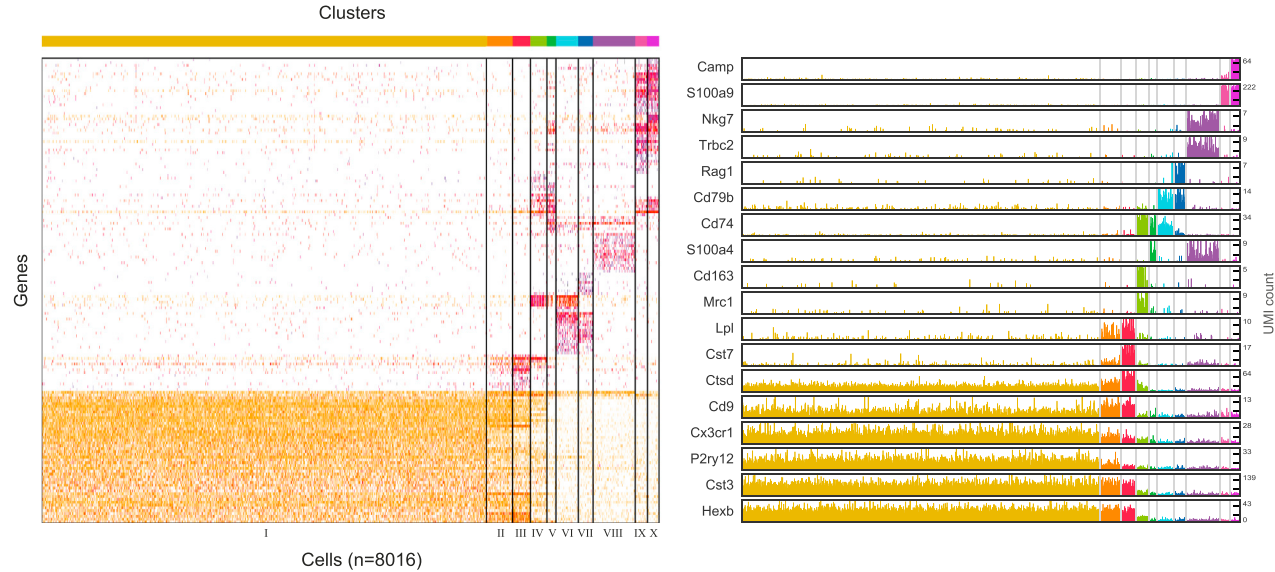
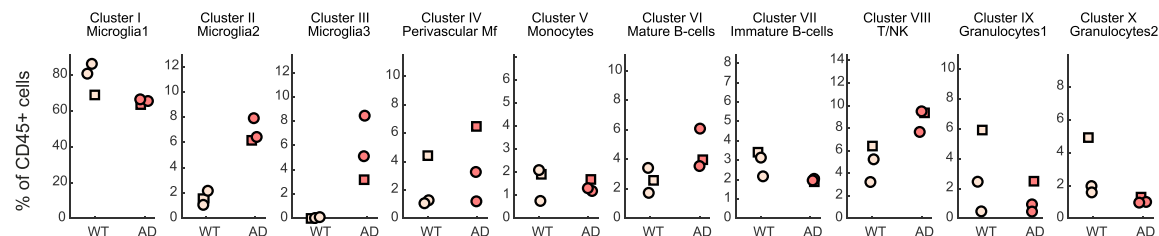
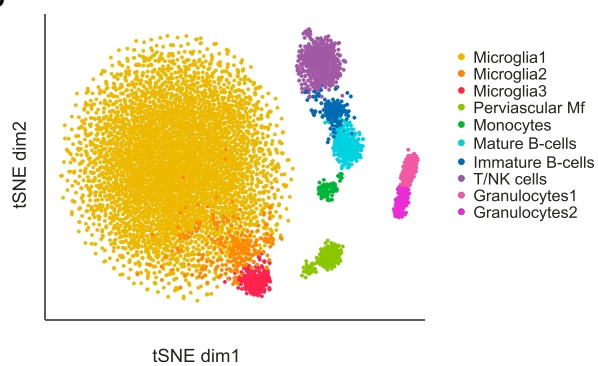
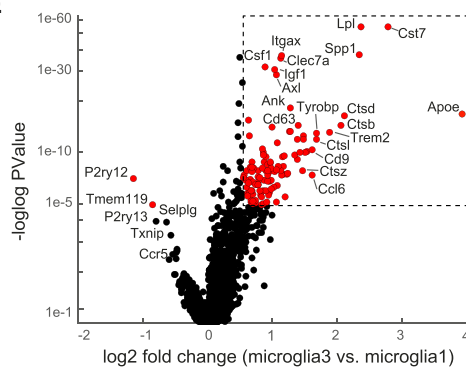
Alzheimer's disease (AD) is a detrimental neurodegenerative disease with no effective treatments. Due to cellular heterogeneity, defining the roles of immune cell subsets in AD onset and progression has been challenging. Using transcriptional single-cell sorting, we comprehensively map all immune populations in wild-type and AD-transgenic (Tg-AD) mouse brains. We describe a novel microglia type associated with neurodegenerative diseases (DAM) and identify markers, spatial localization, and pathways associated with these cells. Immunohistochemical staining of mice and human brain slices shows DAM with intracellular/phagocytic A $\beta$  particles. Single-cell analysis of DAM in Tg-AD and triggering receptor expressed on myeloid cells 2 (Trem2)<sup>-/-</sup> Tg-AD reveals that the DAM program is activated in a two-step process. Activation is initiated in a Trem2-independent manner that involves downregulation of microglia checkpoints, followed by activation of a Trem2-dependent program. This unique microglia-type has the potential to restrict neurodegeneration, which may have important implications for future treatment of AD and other neurodegenerative diseases.

## INTRODUCTION

The CNS, as an immune privileged site, has evolved unique mechanisms to allow it to benefit from its resident myeloid cells, microglia, as well as from communication with the systemic immune system (Hanisch and Kettenmann, 2007; Louveau et al., 2015; Quan and Banks, 2007; Schlegelmilch et al., 2011; Schwartz and Shechter, 2010; Sierra et al., 2014; Tremblay

et al., 2011; Ziv et al., 2006). In the mouse embryo, microglia migrate from the yolk sac to the CNS at embryonic days 8–9, undergo a stepwise program of development that is synchronized with the brain developmental process, and subsequently acquire a stable phenotype essential for the brain protection and homeostasis (Ginhoux and Prinz, 2015; Matcovitch-Natan et al., 2016). Microglia immune activity is restrained by dedicated immune inhibitory pathways that suppress unwanted inflammatory responses and tissue destruction that are often associated with immune activation (Hanisch and Kettenmann, 2007). These checkpoint mechanisms include direct inhibitory interactions of microglia with neurons through the receptor-ligand pairs CX3CL1-CX3CR1 and CD200-CD200R, soluble molecules present in the CNS milieu (e.g., transforming growth factor  $\beta$  [TGF- $\beta$ ]), and intracellular regulators such as the transcription factor MafB (Butovsky et al., 2015; Kierdorf and Prinz, 2013; Lauro et al., 2015; Matcovitch-Natan et al., 2016; Ransohoff and Cardona, 2010). Nevertheless, these mechanisms may be disadvantageous under extreme conditions when reparative microglial activity is needed.

Alzheimer's disease (AD) is an age-related neurodegenerative disease characterized by progressive memory decline and cognitive dysfunction, often manifested histologically by the parenchymal deposition of amyloid-beta (A $\beta$ ) plaques, the formation of neurofibrillary tangles and neuroinflammation (Hardy and Selkoe, 2002; Holtzman et al., 2011). Numerous studies reported conflicting results regarding the contribution of systemic immunity, recruited monocytes, and tissue-resident microglia to AD onset and disease progression (Baruch et al., 2016; Deardorff and Grossberg, 2017; Guillot-Sestier et al., 2015; Jay et al., 2015; Koronyo et al., 2015; Lai and McLaurin, 2012; Simard et al., 2006; Wang et al., 2016). Some reports show that under such conditions, microglia acquire pro-inflammatory activity, which has been associated with disease escalation (Heppner et al., 2015; Tejera and Heneka, 2016; Wang et al., 2015; Yamasaki et al., 2014). However, the current methods, analyzing bulk cell populations isolated based on a small set of surface markers, might be limited in resolving the heterogeneity, niche specificity, and

**A****B****C****D****E**

(legend on next page)

complexity of immune cell types within the CNS (Elowitz et al., 2002; Geissmann et al., 2010; Hume, 2008). Single-cell genomic technologies enable unbiased characterization of immune cell types and states, transitions from normal to disease and response to therapies, supporting comprehensive genome-wide sampling by single-cell RNA sequencing (RNA-seq) as an effective tool to systematically resolve immune heterogeneity in AD (Deng et al., 2014; Grün et al., 2015; Gury-BenAri et al., 2016; Jaitin et al., 2014; Junker and van Oudenaarden, 2014; La Manno et al., 2016; Mass et al., 2016; Matcovitch-Natan et al., 2016; Paul et al., 2015; Treutlein et al., 2014; Zeisel et al., 2015). Single-cell analysis can further identify potential markers, pathways, and regulatory factors, promoting testable hypotheses to elucidate molecular mechanisms of immune regulation in AD (Jaitin et al., 2016; Matcovitch-Natan et al., 2016; Paul et al., 2015).

Taken together, it is still not clear whether microglial function in neurodegenerative diseases is beneficial but insufficient, or whether these cells are effective at early disease stages but lose their efficacy or even become detrimental later on. Importantly, the pathways and molecular mechanisms of microglia activity at the different stages of AD thereby remain controversial. Here, we combine massively parallel single-cell analysis with chromatin profiling, single-molecule FISH (smFISH), immunohistochemistry, genetic perturbation, and computational modeling to comprehensively characterize de novo the involvement of the immune system in AD progression. Using a mouse model of AD that expresses five human familial AD gene mutations (5XFAD), we uncover a disease-associated microglia (DAM) subtype. Further analysis identifies DAM in another mouse model of neurodegenerative disease, namely, amyotrophic lateral sclerosis (ALS). Our results also depict the pathways activated in DAM, which have been associated with known AD risk factors, but not specifically attributed to microglia. Using sub-tissue-focused single-cell RNA-seq and smFISH, we identified the spatial location of DAM in proximity to A $\beta$  plaques. Immunohistochemical staining showed an increased number of microglia that are positively stained for intracellular A $\beta$  particles and DAM-markers in both 5XFAD mice and in human AD postmortem brains. Comparing triggering receptor expressed on myeloid cells 2 (Trem2)<sup>-/-</sup>5XFAD with Trem2<sup>+/+</sup>5XFAD mice revealed that initial DAM activation, that includes upregulation of Tyrobp, Apoe, and downregulation of microglia checkpoint genes (e.g., Cx3cr1 is Trem2-independent, but full activation of the DAM program including phagocytic and lipid metabolism activity is a consequential event that is Trem2-dependent. Over-

all, our study identifies a potential protective microglia type associated with neurodegeneration and outlines a general framework for studying the involvement of the immune system in AD pathology.

## RESULTS

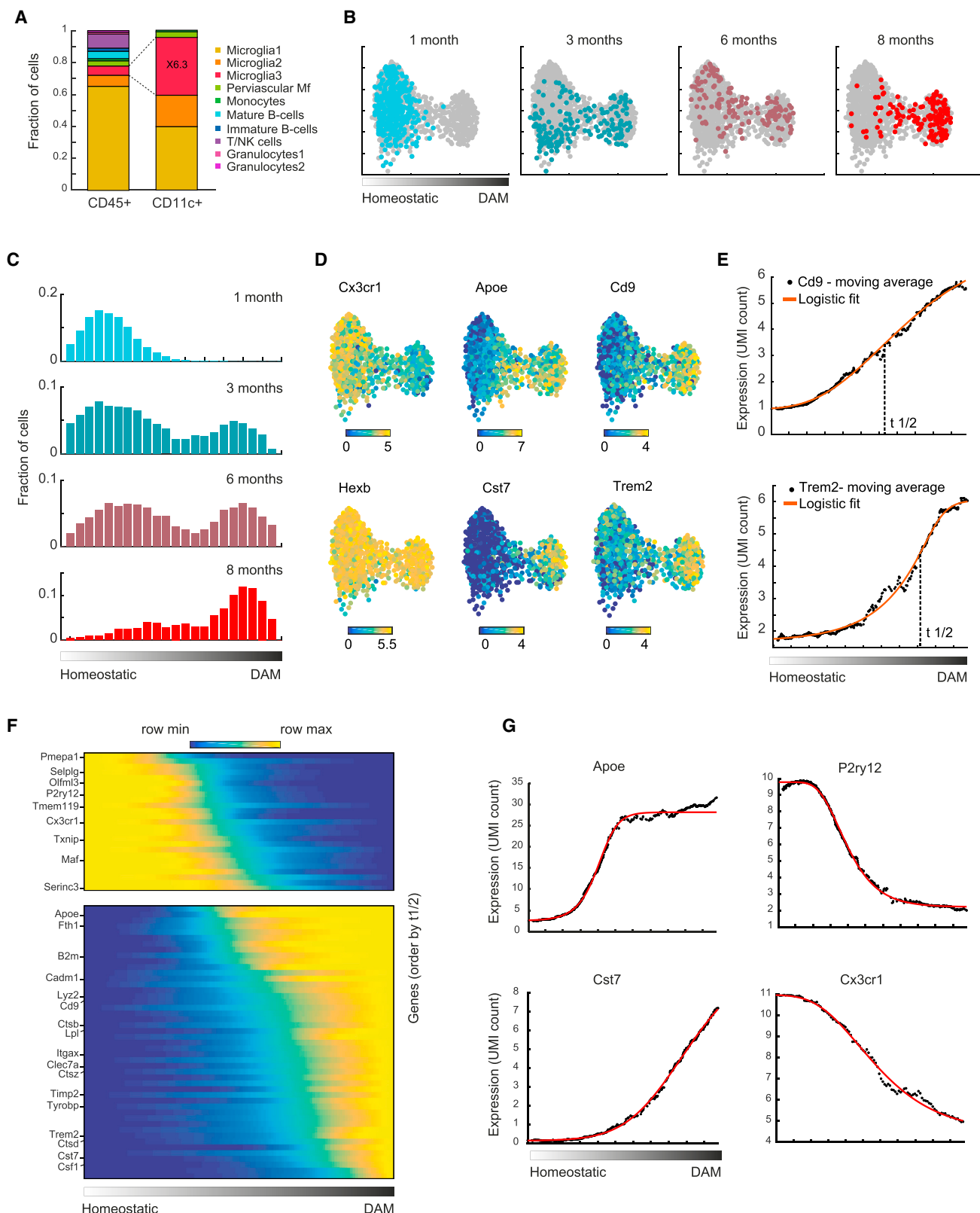
### Identification of a Unique Microglia Type Associated with Alzheimer's Disease

Current characterization of immune cells involved in AD has been obtained from populations sorted according to a small set of canonical cell-surface markers. Therefore, the observed gene expression signatures may obscure the presence of additional immune cell types and overlook the composite picture of related and dynamic subsets in the brain. To de novo characterize the immune cell types and states involved in AD, we first sorted all immune cells (CD45 $^{+}$ ) from brains of 5XFAD, a commonly used AD transgenic mouse model that expresses five human familial AD gene mutations (Oakley et al., 2006), compared with age- and sex-matched wild-type controls, and performed massively parallel single-cell RNA-seq (MARS-seq) (Jaitin et al., 2014) (Figures 1A and S1A). In order to link between the canonical surface markers to the genome-wide expression profiles, we used an index-sorting strategy that allowed for retrospective analysis of surface marker combinations of each individual cell (see the STAR Methods). Unsupervised graph-based clustering (PhenoGraph) (Levine et al., 2015) of all 8,016 single cells sorted from six wild-type and AD mice, created a detailed map of the ten most transcriptionally distinct subpopulations (Figures 1B and S1B; Table S1). These distinct immune subpopulations were based on cluster-specific expression patterns of the 500 most variable genes, allowing de novo identification of rare subpopulations. Our analysis identifies a monocyte state, represented in cluster V, a perivascular macrophage group in cluster IV (Zeisel et al., 2015), several lymphocytes sub groups (B cells, T cells, natural killer [NK] cells; clusters VI–VIII), granulocytes (IX–X), and a large group of microglia cells (cluster I; Figures 1B and S1B). Surprisingly, our analysis also identifies two small groups of cells, clusters II (4.2%) and III (2.8%), which displayed expression of microglial genes (Cst3 and Hexb) with an additional unique signature of lipid metabolism and phagocytic genes such as Apolipoprotein E (Apoe), lipoprotein lipase (Lpl), and Cystatin F (Cst7) (Figures 1B and S1B).

Examining the contribution of wild-type versus AD backgrounds to each group of cells revealed a similar percentage of cells in perivascular macrophages, monocytes, group I

### Figure 1. Single-Cell RNA-Seq Reveals a Unique Microglia Type Associated with Alzheimer's Disease

- (A) Schematic diagram showing the isolation of single cells from whole brains of WT and Tg-AD (AD) mice for massively parallel single-cell RNA-seq (MARS-seq) yielding genotype to cellular and molecular phenotype relations.
  - (B) Heatmap showing clustering analysis of 8,016 single cells, featuring 220 most variable genes, from 3 WT and 3 AD 6-month-old mice. The expression level (UMI count, see the STAR Methods) of selected marker genes for each cluster (I–X) is shown on the right.
  - (C) Dot plot showing the percentage of WT (beige) or AD (red) cells out of the total CD45 $^{+}$  cells in each of the clusters identified in (B). Each data point, circle (female) or square (male), represents an independent single-cell experiment performed on an individual animal.
  - (D) t-SNE plot of the 8,016 single cells depicting the separation into the ten clusters as shown in (B).
  - (E) Volcano plot showing the fold change of genes (log2 scale) between DAM (microglia3) to homeostatic microglia (microglia1) from the AD male brain (x axis) and their significance (y axis, -log<sub>10</sub> scale). See Table S2. Highly significant genes are indicated by a red dot. p values were determined by Mann-Whitney U test with FDR correction. Individual female animals are shown in Figure S1D.
- See also Table S1.



(legend on next page)

microglia, granulocytes, and slight differences between the wild-type (WT) and the AD model in lymphocytes (Figure 1C). Strikingly, group II and III microglia represent distinctive microglia states observed in AD but not in the WT background, and we define this state as disease-associated microglia (DAM). Projection of the cells using t-distributed stochastic neighbor embedding (t-SNE), localizes the DAM group in proximity to the microglia territory and distinct from the monocytes and perivascular macrophages (Figures 1D and S1C). Closer examination of the profiles and key marker genes of homeostatic microglia to group II and III DAM revealed similarity to the microglial program (e.g., Hexb and Cst3; Figures 1B, S1B, and S1C). However, DAM also demonstrate significant changes in gene expression compared with microglia such as reduction in the expression levels of several microglia homeostatic genes, including the purinergic receptors P2ry12/P2ry13, Cx3cr1, and Tmem119 (Figures 1B, 1E, and S1D) (Butovsky et al., 2015; Haynes et al., 2006; Hickman et al., 2013; Merino et al., 2016; Mildner et al., 2017). Many more genes are upregulated in DAM including several known AD risk factors such as Apoe (Corder et al., 1993), Ctsd (Paz-Y-Miño et al., 2015), Lpl (Scacchi et al., 2004), Tyrobp (Pottier et al., 2016), and Trem2 (Guerreiro et al., 2013; Jonsson et al., 2013) (Figures 1E and S1D; Table S1). Comparison of homeostatic microglia to group II and III DAM shows that the expression changes for many of the DAM-specific genes are in the same trajectory but more pronounced in group III, which may suggest that group II is an intermediate state between homeostatic microglia and group III DAM (Figures 1B and 1D). Gene set enrichment analysis (GO) of DAM-specific genes revealed significant involvement ( $p < 1 \times 10^{-14}$ ) in lysosomal/phagocytic pathways, endocytosis, and regulation of the immune response (Figure S1E).

### Disease-Associated Microglia Dynamics during AD Progression

AD is a progressive disease with gradual increase in neuronal death and loss of cognitive function (Ballard et al., 2011). Identifying the relevant changes in DAM regulation along the course of the disease could shed light on the molecular mechanisms of DAM regulation and potentially suggest new therapeutic targets. AD typically progresses in three general stages; early-stage, mild-moderate, and severe (Reitz and Mayeux, 2014). In the 5XFAD AD model, these stages are accelerated: high levels of intraneuronal aggregated  $\beta$ -amyloid start to appear at around 1.5 months of age and amyloid and plaque deposition at

2–3 months of age. Neuronal loss and deficits in spatial learning initiate at around 6 months and severe cognitive dysfunction is observed at 7–8 months of age (Kimura and Ohno, 2009; Oakley et al., 2006). We therefore performed single-cell RNA-seq in whole brains of 5XFAD mice at 1, 3, 6, and 8 months of age.

In order to enrich for the rare DAM cells over other immune populations, we used the single-cell data to identify potential markers. We identified CD9, Itgax (CD11c), Clec7a, and CD63 as potential DAM markers (Figure 1E; Table S2) and sorted 1,358 CD11c<sup>+</sup> microglia from the different time points along disease progression (Figure S2A). Comparing CD11c<sup>+</sup>-sorted microglia from 6-month-old AD mice with the corresponding CD45<sup>+</sup> selection revealed 6.3 $\times$  enrichment of DAM (Figures 2A and S2B). Index sorting of CD11b cells demonstrate that there are no cells with a DAM signature that are CD11c negative (Figure S2C). However, projection of CD11c<sup>+</sup> cells onto our CD45<sup>+</sup> map revealed that CD11c<sup>+</sup> cells are an heterogeneous cell population that include a mixture of various myeloid cells, including microglia, perivascular macrophages, and monocytes (Figure S2D), which may limit biological relevance of bulk analysis using CD11c as a marker for AD (Chiu et al., 2013; Hickman et al., 2013; Holtzman et al., 2015; Kamphuis et al., 2016; Landel et al., 2014; Orre et al., 2014a, 2014b; Wang et al., 2015). We therefore in silico removed all myeloid contaminants from the time course data and analyzed the remaining 893 DAM and microglial cells. To model the dynamics of microglia along disease progression we generated a k-nearest neighbors graph (kNN) of microglia cells from all major disease stages. Two-dimensional projection of the graph identifies homeostatic microglia and DAM on the two extremes of the graph with an intermediate group of cells connecting the two states (Figure 2B). This analysis demonstrated that microglia in the AD model, and not in the WT, display a transition from homeostatic microglia to DAM population as a function of disease progression (Figures 2B, 2C, and S2E). While most genes do not change their expression as a function of microglia transition (Hexb), some genes display a decrease in gene expression along this activation axis (Cx3cr1) and some show an increase in their gene expression (Apoe, Lpl, CD9, Cst7, Trem2) (Figure 2D; Table S3). In order to define the temporal transcriptional changes leading to DAM formation, we generated a mathematical model based on a generalized logistic function to describe the temporal changes in gene expression (Figure 2E; see the STAR Methods). Our model depicts the molecular order of events in which microglia are switching from the homeostatic state to DAM (Figure 2F;

**Figure 2. Disease-Associated Microglia Display Dynamics of Activation during AD Progression**

- (A) Bar plot showing the relative distribution of each cluster identified in Figure 1B with CD45<sup>+</sup> sorting (left, 1,045 cells) compared to CD11c<sup>+</sup> microglia (CD45<sup>low</sup>CD11b<sup>+</sup>) enrichment (right, 186 cells).
  - (B) kNN projection of the 893 single cells taken from the AD mouse at each time point along disease progression (1, 3, 6, 8 months; color) on the background of all microglia (gray). x axis refers to the transition axis from homeostatic microglia to DAM.
  - (C) Bar plots quantifying the percentage of cells presented in (B) along the activation axis.
  - (D) Projection of key marker genes onto the graph plot of microglia, as shown in (B). Color bar below each plot represents color scale level (log2 UMI counts).
  - (E) Graph displaying sliding window smoothed expression (UMI counts,  $w = 20$ ) of selected markers (CD9, Trem2) in each cell along the activation axis with a generalized logistic curve fit (marked in orange).  $t_{1/2}$  represents half maximal response.
  - (F) Heatmap showing the kinetics of DAM differential genes ordered by their  $t_{1/2}$ . Top panel contains downregulated genes and lower panel contains upregulated genes. See Table S4.
  - (G) Graphs showing the ordering of key marker genes along the transition axis.
- See also Figure S2 and Table S3.

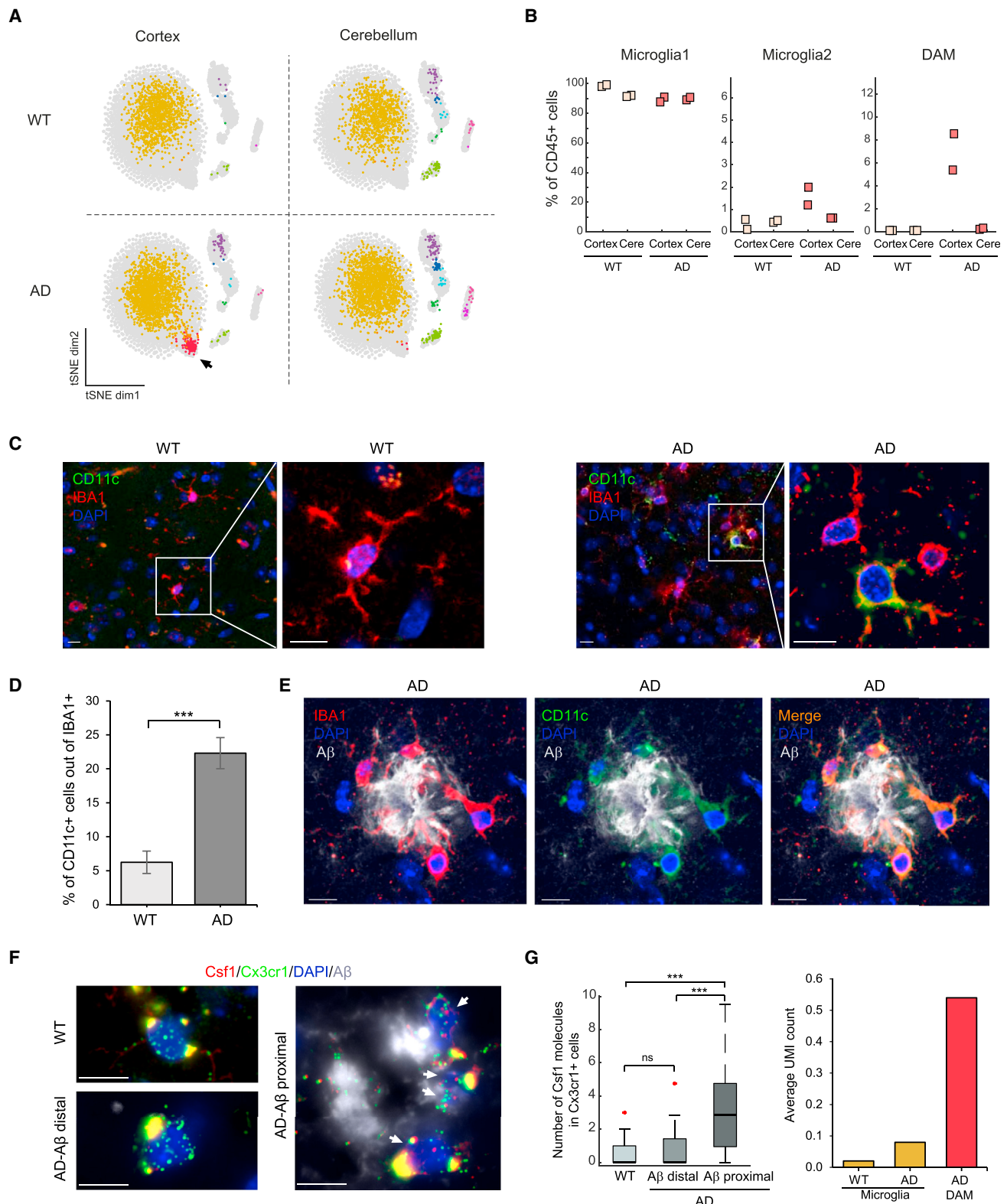


**Figure 3. DAM Are Localized Near the AD Plaques**

(A) Projection of 6,347 single cells isolated from either cortex (3,247) or cerebellum (3,100) collected from brains of 6-month-old WT and Tg-AD (AD) mice ( $n = 2$  for each area) onto the t-SNE plot of Figure 1D, showing the spatial location of DAM in the cortex of AD mice (indicated by an arrow).

*(legend continued on next page)*

**Table S4**). Analysis of genes in the different disease stages (Figure 2B) revealed that initial transition events are more frequent in earlier disease stages (3 months) and include downregulation of P2ry12/13 and Cx3cr1 and upregulation of Tyrobp and Apoe. Later regulatory events are more frequent in advanced stages of the disease (8 months) and include upregulation of Cst7, Lpl, and Trem2 (Figures 2F and 2G).

Chromatin plays a major regulatory role in cell-type-specific functions and response (Winter et al., 2015). Transcriptional changes from latent enhancers, rather than previously established enhancers, could resolve whether the DAM program is an immediate transcriptional response or a less anticipated response that requires more complex chromatin rearrangements (Ostuni et al., 2013). We therefore used a high sensitivity method for chromatin immunoprecipitation followed by sequencing (iChIP) comparing microglia and DAM enhancers in WT and AD mouse model (Lara-Astiaso et al., 2014). We observed a highly similar ( $r^2 = 0.86$ ) global pattern of histone 3 lysine 4 di methyl regions (H3K4me2), which marks promoter and enhancer regions. Focusing on DAM-specific genes, we observed active H3K4me2 regions in both the microglia and DAM demonstrating that the DAM program is already primed in homeostatic microglia (Figures S2F and S2G).

#### DAM Are Localized near AD Plaques

Our single-cell analyses were obtained from immune cells isolated from whole brains including the meninges and parenchyma of AD involved (e.g., cortex) and uninvolving (e.g., cerebellum) brain regions. In order to spatially orient the immune cell compositions within different brain regions, we repeated the single-cell sorting experiments on dissected cortex and cerebellum of 6-month-old AD and WT mice and compared the immune composition of these two regions using single-cell RNA-seq of all immune (CD45<sup>+</sup>) cells. Analyzing 6,347 cells from four AD and WT mice, we found that DAM are located within the cortex, but not the cerebellum of AD mice (Figures 3A, 3B, and S3A). Using the rich molecular characteristics of DAM, we further performed immunohistochemistry staining and single molecule fluorescence *in situ* hybridization (smFISH). We focused on differentially expressed DAM markers and anti-A $\beta$  plaque labeling. Cortex staining for IBA-1, a classical homeostatic microglial

marker, together with CD11c, shows a small overlap (6%) within WT mice. In contrast, we identified a significant population (22.3%) of microglia that co-expresses these markers in 6-month-old AD mice (Figures 3C and 3D). Examining the expression of IBA-1 positive with CD11c-positive cells in AD transgenic mice stained for A $\beta$  plaques shows that microglia co-express these markers in proximity to plaque foci (Figure 3E). Further, CD11c is co-expressed with TIMP2, a marker for DAM, on microglia cells in AD mice (Figure S3B). Probing for the spatial distribution of DAM-specific genes, Csf1 and Lpl, using smFISH, shows significant overlap of these two genes within microglia cells near the A $\beta$  plaques (Figures 3F, 3G, S3C, and S3D). This attributes our identified DAM population to cells localized in the vicinity of the A $\beta$  plaques.

#### DAM Are Phagocytic Cells Conserved in Human and Other Neurodegenerative Diseases

DAM express high levels of phagocytic and lipid metabolism pathways. We therefore examined whether DAM would phenotypically show high incidence of intracellular phagocytic particles of A $\beta$ . We immunostained brain slices with Lpl, a DAM-specific gene previously identified as an AD risk factor, together with histological staining using Thioflavin-S, which labels both extracellular and intracellular forms of A $\beta$  (Rajamohamedsait and Sigurdsson, 2012). Analysis of these brain slices show that microglia containing Thioflavin-S-labeled particles are mostly clustered in close vicinity of A $\beta$  plaques, from 1.8% of microglia in regions with low density of plaques to 60.6% in regions with high density of plaques (Figures 4A and 4B). These phagocytic microglia showed nearly complete co-expression of the DAM marker Lpl (95.8%; Figure 4B). Further, in order to examine if DAM cells are conserved in human, we used the same strategy and stained human postmortem brains and age-matched non-AD controls for A $\beta$  and Lpl. Our analysis shows a very strong overlap between Lpl-positive microglia, predominantly around A $\beta$  plaques, in AD postmortem brain samples; such cells could not be detected in non-AD brain slices (Figures 4C and S4A).

To examine the presence of DAM in other neurodegenerative conditions, we performed single-cell analysis of all immune cells from spinal cords of a mouse model of ALS, a neurodegenerative disease characterized by the progressive degeneration of motor

(B) Dot plot quantification for microglia clusters I–III (microglia1, microglia2, and DAM) showing the percentage of WT (beige) or AD (red) cells out of the total CD45<sup>+</sup> cells in each of the clusters identified in (A). Each data point (square, male) represents an independent single-cell experiment performed on an individual animal.

(C) Representative immunofluorescence images of CD11c (green) and microglia (IBA-1, red) in cortical sections of 6-month-old WT and Tg-AD (AD) mice. Cell nuclei are shown in blue (DAPI). Scale bar, 10  $\mu$ m.

(D) Bar plot showing quantification of CD11c<sup>+</sup> microglia out of total microglia based on overall 944 cells counted in the cortex of WT and AD mice. \*\*\* <0.001. Error bars represent SEM.

(E) Immunofluorescence imaging of CD11c-positive microglia together with A $\beta$  plaques (gray). Scale bar, 10  $\mu$ m.

(F) smFISH of mRNA molecules for Cx3cr1 (green), a marker for homeostatic microglia, and Csf1 (red), a DAM marker, together with A $\beta$  plaques immunostaining (gray) and DAPI staining (blue) in intact brain tissue taken from 6-month-old WT and AD mice. Imaging of AD mouse brains was performed in a region with low density of A $\beta$  plaques (AD-A $\beta$  distal; bottom left) and in a region with a high density of A $\beta$  plaques (AD-A $\beta$  proximal; right). Large yellow blobs are cytoplasmic auto-fluorescent objects. Scale bar, 5  $\mu$ m.

(G) Left: quantification of the number of Csf1 molecules in microglia. Horizontal lines are medians, boxes demarcate the 25–75 percentiles; vertical lines are 1.5 times the interquartile range. Red plus signs represent outliers. Right: average UMI count obtained from the single-cell RNA-seq data. Quantification was done based on the overall number and size of A $\beta$  plaques in each field. n(WT) = 39, n(AD-A $\beta$  distal) = 17, n(AD-A $\beta$  proximal) = 66, \*\*\* <0.001. ns, non-significant. Error bars represent SEM.

See also Figure S3.

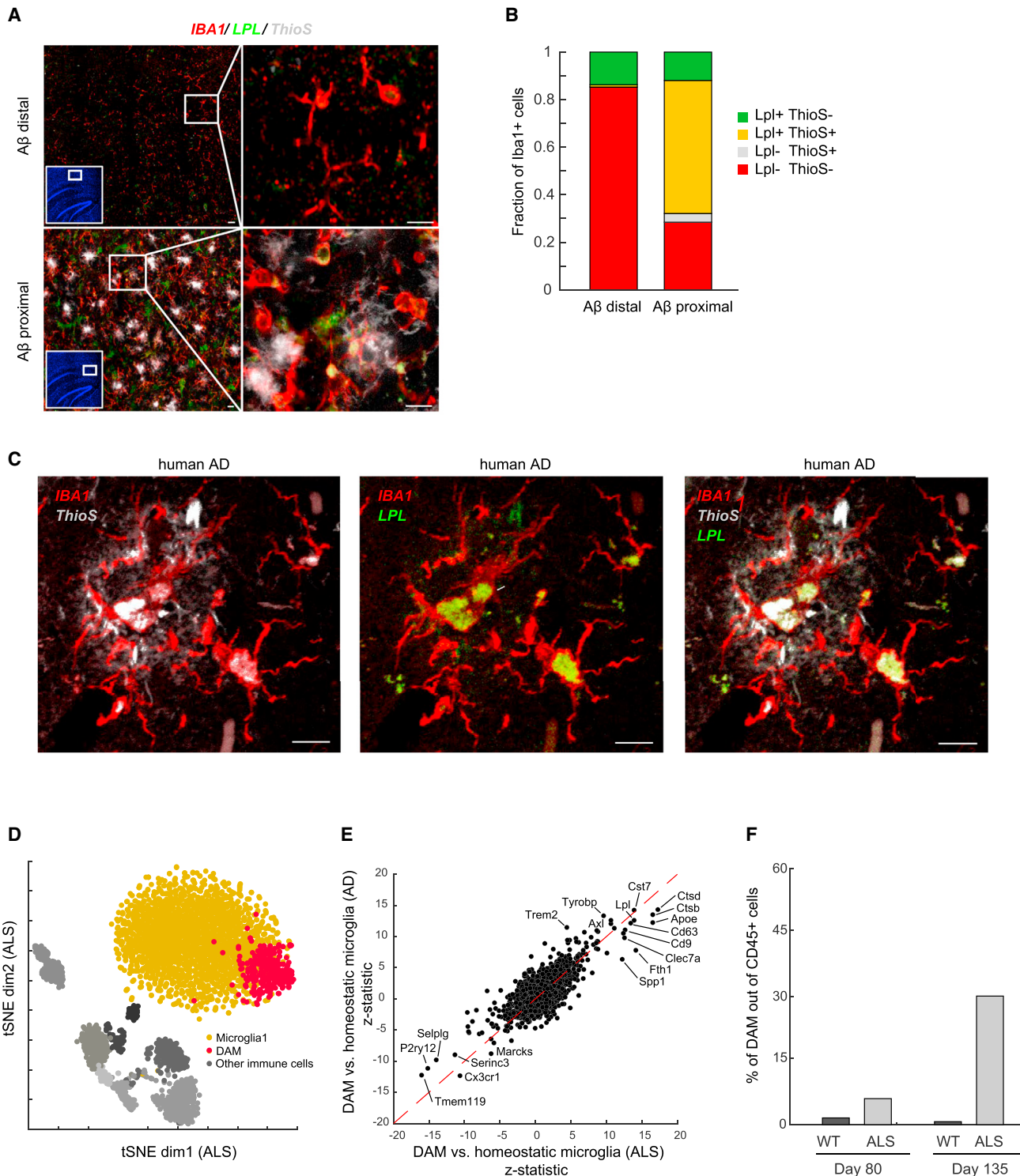


**Figure 4. DAM Are Phagocytic Cells Conserved in Human and Other Neurodegenerative Diseases**

(A) Representative images from brain regions with low and high density of A $\beta$  plaques (A $\beta$  distal, top; A $\beta$  proximal, bottom) of 6-month-old Tg-AD mice, stained for a DAM marker gene (LPL; green), IBA-1 (microglia, red), and Thioflavin-S (ThioS; A $\beta$ , gray). Small squares (insets) represent position of images by cell nuclei staining (DAPI, blue).

(B) Bar plot showing the fraction of IBA-1 $^{+}$  cells (microglia) in A $\beta$  distal and proximal brain regions, stained for LPL and ThioS.

(legend continued on next page)

neurons in the spinal cord (McCombe and Henderson, 2011). We sorted 3,194 CD45<sup>+</sup> cells from the spinal cords of mSOD1 (G93A) mice, a transgenic ALS mouse model mimicking the familial human disease (Gurney et al., 1994), at early (day 80) and late (day 135) disease progression stages and performed single-cell RNA-seq. Analysis revealed similar immune cell populations to those identified in the WT and AD mice with different proportions (Figures 4D and S4B; Table S5). The majority of the cells were represented by microglia, expressing the relevant markers such as Hexb and Cx3cr1 (Figures 4D, S4B, and S4C). Importantly, we also observed a distinct group of cells with microglia characteristics in the spinal cords of ALS mice but not in the WT mice (Figures 4D and S4B). These cells display an expression profile that is highly similar to the DAM observed in the AD model, including upregulation of Trem2, Tyrobp, Lpl, and Cst7 as well as downregulation of P2ry12 and Cx3cr1 (Figures 4E and S4B–S4D; Table S6). Of the total CD45<sup>+</sup> cells, the percentage of DAM increases from 6% at day 80 to nearly 30% by day 135 (Figure 4F), which points to further accumulation of DAM during ALS progression. To further generalize the regulation of DAM in various neurodegenerative conditions, we performed single-cell RNA-seq on 631 CD11b<sup>+</sup> immune cells isolated from whole brains of aged (20-month-old) mice compared with young (7-week-old) mice. Analysis of the microglia cells revealed a large increase of the DAM population in the aged mice compared with young adults, from non-detected to 3%, respectively (Figure S4E). These results suggest that DAM actively participate in the dismantling and digestion of the amyloid plaques and are conserved from mouse to human neuropathology.

### DAM Activation Is Initiated by a Trem2-Independent Mechanism

In order to better understand the regulatory mechanisms of DAM, we further analyzed the single-cell data, seeking potential regulators that may trigger DAM activation. Among them, we identified Tyrobp (Tyro protein tyrosine kinase binding protein) and Trem2 (triggering receptor expressed on myeloid cells 2), which form a signaling complex; both components are strongly induced in DAM (Figure 1E; Table S1) (Colonna and Wang, 2016; Painter et al., 2015; Wang et al., 2015). Mutations in Trem2 were associated with risk factors in AD (Colonna and Wang, 2016; Guerreiro et al., 2013; Jonsson et al., 2013) and Trem2 deficiency in an AD mouse model accelerated A $\beta$  plaque accumulation and neuronal loss (Jay et al., 2015; Wang et al., 2015, 2016; Yuan et al., 2016). To decipher the role of Trem2 in DAM activation, we performed single-cell RNA-seq of DAM, using CD11c and CD11b enrichments, from whole brains of Trem2<sup>+/+5XFAD</sup> and Trem2<sup>-/-5XFAD</sup> mice together with matched WT and Trem2<sup>-/-</sup> controls, altogether 3,864 cells.

Following digital sorting and removal of monocytes contaminants, the remaining microglia cells were clustered using a kNN graph and projected on a two-dimensional space, displaying a spectrum of transcriptional states from homeostatic microglia toward the DAM state (Figure 5A). Similar to our single-cell analysis of AD mice (Figure 1B), we observed three distinct microglia groups: homeostatic, intermediate state, and DAM (Figure 5A). Interestingly, the intermediate state, which expressed only a partial set of the DAM program, Tyrobp, Apoe, B2m, and Ctsd, but not the majority of the lipid metabolism and phagocytic pathway genes (e.g., Lpl), was much more abundant in the Trem2 knockout experiment.

Overlaying the mice genotype on our model shows that both WT and Trem2<sup>-/-</sup> contain only homeostatic microglia, expressing high levels of microglia marker genes (e.g., Cst3, Hexb, and Cxc3cr1) (Figures 5B, 5C, and S5). Trem2<sup>+/+5XFAD</sup> displayed a similar DAM program to that observed before (Figures 1B, 2B, 5B, and 5C). Strikingly, in the Trem2<sup>-/-5XFAD</sup> background, the mice brains were completely depleted of DAM and instead accumulated a large number of cells in the intermediate state, demonstrating that the DAM program progresses through Trem2-dependent and Trem2-independent pathways (Figures 5B, 5D, 5F, and S5; Table S7). A similar intermediate DAM state is observed in the Trem2<sup>+/+5XFAD</sup> at a smaller frequency (Figure 5E), but unlike in the Trem2<sup>-/-</sup> background, most cells proceed and activate the full DAM program (Figures 5B, 5D, and S5). This analysis suggests that DAM are generated through a two-step mechanism of activation of homeostatic microglia (Figure 6). An initial activation through an unknown mechanism leads to an intermediate state (stage 1) in a Trem2-independent mechanism, which critically involves reduction in the expression of homeostatic microglia checkpoint genes (e.g., Cx3cr1 and P2ry12/P2ry13) and upregulation of genes such as B2m, Apoe (associated with AD progression) (Castellano et al., 2011), and the Trem2 adaptor Tyrobp (Figures 5 and 6). This intermediate DAM program can be further activated by a secondary activation signal that is Trem2-dependent (stage 2) and involves upregulation of phagocytic and lipid metabolism genes such as Cst7 and Lpl (Figures 5 and 6). Interestingly, no cells with a Trem2-dependent program are observed without the Trem2-independent program, which suggests that DAM activation is a mechanistically coupled temporal event that must first be initiated in a Trem2-independent pathway, followed by activation of the Trem2-dependent program.

### DISCUSSION

Immune cells and pathways are frequently implicated in neurodegenerative conditions. For the last decades, the nature of

(C) Representative image of postmortem AD human hippocampal section ( $n = 5$ ) stained for LPL (green), microglia (IBA-1, red), and Thioflavin-S (ThioS) for A $\beta$  (gray). Four out of five samples stained positive for microglia expressing Lpl labeled with A $\beta$  particles. Scale bars, 10  $\mu$ m.

(D) t-SNE plot of 3,194 single cells taken from the spinal cord of WT and ALS mice at ages 80 days and 135 days ( $n = 2$  from each age). Microglia are shown in yellow, DAM are indicated in red, and other immune cells are shown in shades of gray.

(E) Scatterplot comparing z statistics (Mann-Whitney U test) for the differentially expressed genes in DAM versus homeostatic microglia in ALS (x axis) versus AD (y axis). See Table S6.

(F) Bar plots comparing the percentage of DAM out of CD45<sup>+</sup> cells taken from the spinal cord of WT and ALS mice at ages 80 days and 135 days. See also Figure S4 and Table S5.

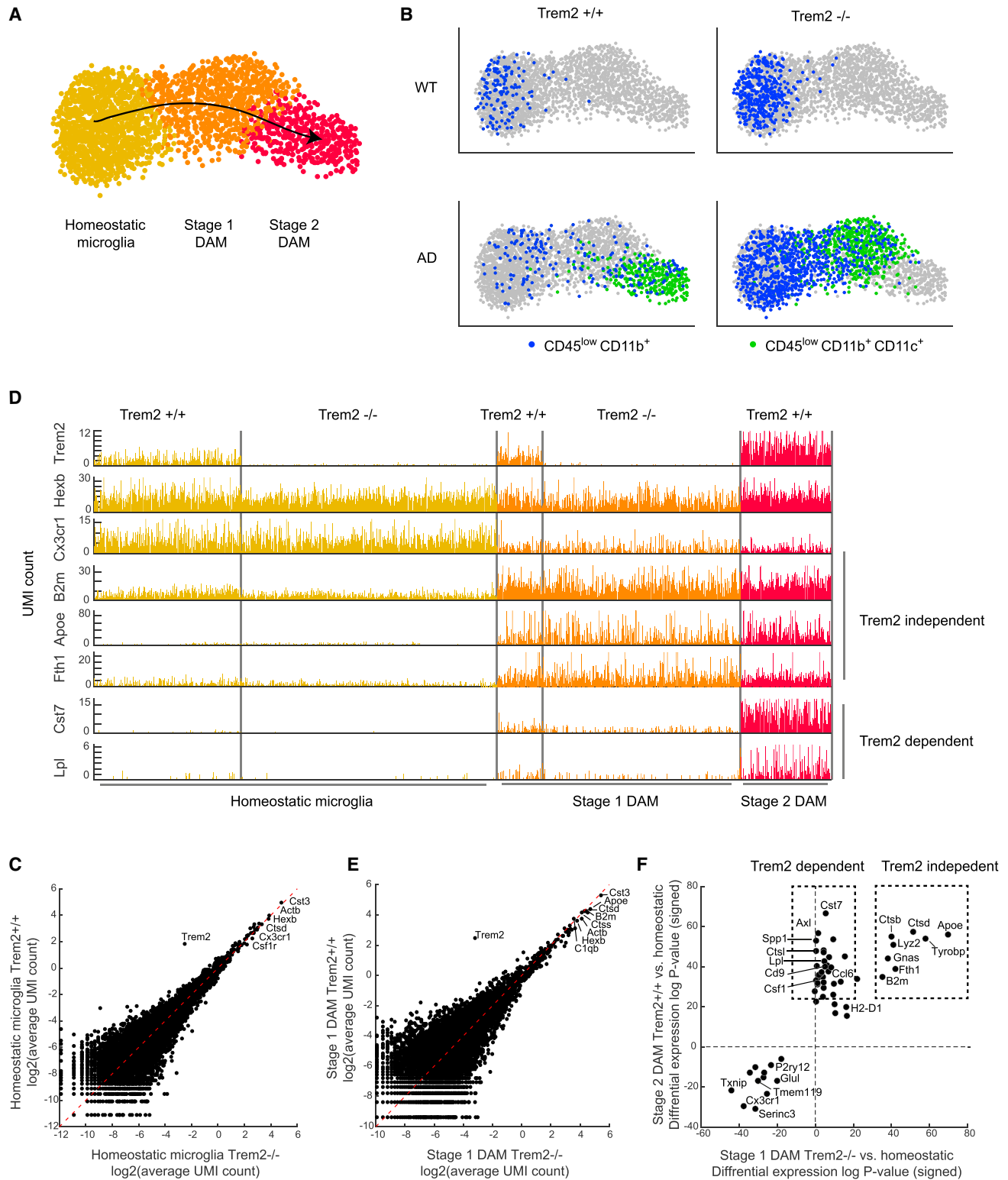


**Figure 5. DAM Activation Is Initiated by a Trem2-Independent Pathway**

(A) Projection of microglia on a kNN graph plot displaying the transition from homeostatic microglia (yellow) to stage 1 DAM (orange) and stage 2 DAM (red). The microglia cells (3,864 cells) were extracted from whole brains of 6-month-old WT, 5XFAD, Trem2<sup>-/-</sup>, and Trem2<sup>-/-</sup>5XFAD mice (n = 4).

(legend continued on next page)

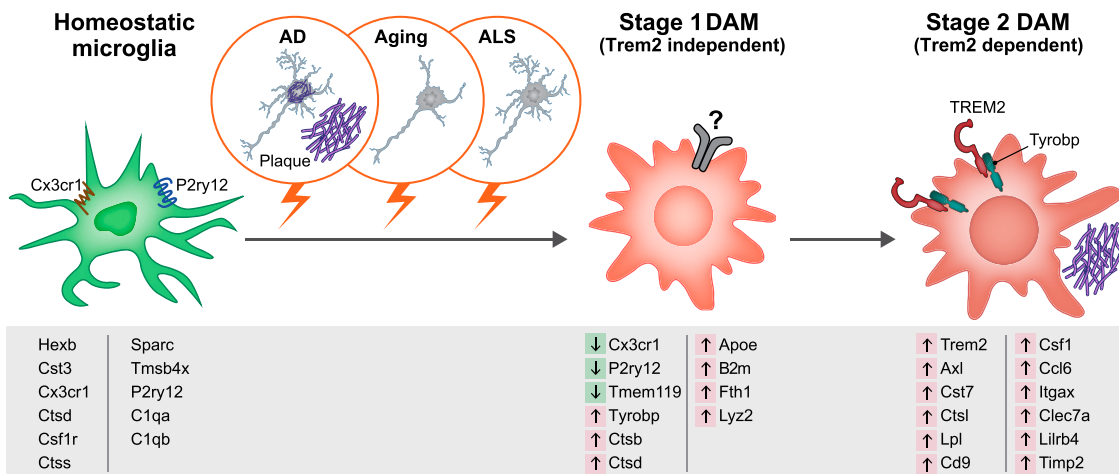


**Figure 6. DAM Are Regulated through a Two-Step Activation Mechanism**

Schematic illustration showing microglia switching from homeostatic to stage 1 DAM (Trem2-independent) and stage 2 DAM (Trem2-dependent) following signals such as those associated with AD pathology, aging, and ALS pathology. Key genes involved in each stage are shown below each condition. Arrows indicate up (red) or down (green) regulation of the gene in the specific stage.

the involvement of microglia, as well as infiltrating immune cells, in the response to brain pathologies have been under constant debate (Chakrabarty et al., 2015; Guillot-Sestier et al., 2015). This was partly due to technical limitations of using marker-based approaches analyzing heterogeneous cell populations, which made it difficult to accurately define the immune cell types and states involved in brain homeostasis and disease. As a result, various innate immune functions have been interchangeably attributed to either microglia or infiltrating blood-derived monocytes. For example, in AD, as in many other neurodegenerative diseases, the local neuroinflammation that is associated with cytotoxicity and disease escalation has often been attributed mainly to microglia (Mosher and Wyss-Coray, 2014; Prinz and Priller, 2014; Wang et al., 2015, 2016; Yuan et al., 2016). In contrast, several studies have attributed a positive role to infiltrating monocytes in the clearance of toxins from the brain (Baruch et al., 2015; Jay et al., 2015; Koronyo et al., 2015; Simard et al., 2006; Thériault et al., 2015).

In the current study, we were able to overcome many of these limitations, and avoid marker-based classifications, by using single-cell RNA sequencing for sampling single immune cells from the brain. Our work establishes a new experimental and conceptual paradigm to accurately analyze the involvement of the immune system in neurodegeneration and other brain pathologies. We identify a novel subtype of protective microglia, DAM, and decipher their dy-

namics along the course of Alzheimer's disease progression. Using immunohistochemistry and smFISH, we found that DAM are spatially associated with sites of AD pathology. Closer examination of the genes expressed by DAM along disease progression revealed elevation of lipid metabolism pathways and phagocytic-related genes, corresponding to the need for plaque clearance in AD. Importantly, the DAM-specific program that we identify includes genes that encode a large number of known risk factors that contribute to disease mitigation. While they were previously identified in AD, they were not functionally linked with microglia. Among these genes is Lpl, whose mutations are associated with an aggressive form of AD (Baum et al., 1999). Our study further shows that the expression of Lpl and additional risk factor genes occurs in the Trem2-dependent phase and attributes a new role for microglia function of these genes in AD. Immunostaining of DAM-specific genes together with A $\beta$  plaques identified enhanced phagocytic activity of DAM cells and their functional conservation in both mice and human AD brains. Single-cell genomic analysis of a large cohort of postmortem brains of AD patients with matched non-AD controls will enable to further identify the role of DAM in AD, and we suspect it will also point to a larger immune heterogeneity than observed in the mouse models.

Trem2 is a microglia-specific immunoreceptor, whose genetic variants are associated with increased risk of neurodegenerative diseases, and homozygous Trem2 loss of function mutations

(B) Projection of the mice genotype on the model from (A). Cells enriched for CD11b (microglia; CD45 $^{low}$ CD11b $^{+}$ ) are marked in blue. Cells enriched for CD11c (DAM; CD45 $^{low}$ CD11b $^{+}$ CD11c $^{+}$ ) are marked in green.

(D) The expression level (UMI counts) of selected marker genes in the different trem2 genotypes at the three microglia states: homeostatic stage 1 DAM, and stage 2 DAM.

(C) Scatterplot showing the average molecules count (log2 scale) of homeostatic microglia in the Trem2 $^{-/-}$  (x axis) compared with the WT (y axis).

(E) Scatterplot showing the average molecules count (log2 scale) of stage 1 DAM in the Trem2 $^{-/-}$ -5XFAD (x axis) compared with the 5XFAD (y axis).

(F) Comparison of log p values of the differential expression of stage 1 DAM versus homeostatic microglia in the Trem2 $^{-/-}$ -5XFAD (x axis) to the differential expression of stage 2 DAM versus homeostatic microglia in 5XFAD (y axis), log p values sign corresponds to upregulation or downregulation.

See also Figure S5 and Table S7.

cause dementia in humans (Colonna and Wang, 2016; Hickman and El Khoury, 2014). In addition, a rare variant of Trem2 has been associated with an increased risk for AD (Guerreiro et al., 2013; Jonsson et al., 2013; Song et al., 2017). In addition to Trem2, we identify strong induction of Tyrobp in DAM. Tyrobp and Trem2 form a signaling complex, associated with A $\beta$  clearance, that could enhance phagocytic activity of microglia and participate in suppression of inflammatory responses by repression of microglia-mediated cytokine production and secretion (Ma et al., 2015). Here, using Trem2<sup>-/-</sup>5XFAD mice, we were able to identify two sequential but distinct stages in DAM activation. The first step, which is Trem2-independent, involves activation of a set of genes, including the Trem2-signaling adaptor Tyrobp, Apoe, and B2m, concomitantly with downregulation of microglia homeostatic factors (e.g., Cx3cr1 and P2ry12/P2ry13). The second phase of DAM activation, including induction of lipid metabolism and phagocytic pathways (e.g., Lpl, Cst7, and CD9), was found to be Trem2-dependent: this transition to fully activated DAM does not occur in the absence of the Trem2 receptor. The fact that expression of this set of genes is associated with phagocytic activity and lipid metabolism, and is dependent on Trem2, supports the recent observation that absence of Trem2 in microglia at the late stage of AD, but not at the early stage, exacerbates disease manifestations (Wang et al., 2015). It is therefore possible that the function of the genes expressed by DAM is needed to mitigate the disease by supporting phagocytosis but it occurs at relatively late stage of the disease. Importantly, none of the genes expressed as part of the DAM program are the primary cause of the disease but rather affect AD timing of onset and rate of progression.

Taken together, our results shed new light on the role of microglia in AD and suggest that at least a sub-population of microglia, the DAM, are beneficial for AD. It is possible that there is a trade-off in brain homeostasis between the number of DAM cells with phagocytic activity and checkpoint mechanisms that keep them under tight control (e.g., CX3CR1 inhibitory signaling). Such checkpoint mechanisms, while essential for the function of microglia, for ensuring their risk-free immune activation, may become a negative factor when this balance is tilted and a strong phagocytic activity is needed in aging or under detrimental genetic backgrounds. In line with this hypothesis, is our current observation that the elevation of genes associated with the first step of DAM activation is tightly coupled with the loss of microglial homeostatic genes. Our results also support the observation that deficiency in CX3CR1 signaling in AD animal models, led to a reduction in A $\beta$  deposition (Lee et al., 2010). It remains to be determined how targeting the microglia-specific inhibitory checkpoints can be used to induce early DAM activation and may be adopted as a therapeutic (or preventive) target to trigger a microglial response against AD plaque pathology, aging, and other neurodegenerative diseases.

Generalizing our study to other neurodegenerative diseases, we found a similar DAM subpopulation in an ALS mouse model. This suggests that DAM are not associated with the specific primary cause of disease pathology or disease etiology, but rather with a general program that is involved in clearance of the protease-resistant misfolded and aggregated proteins that commonly accumulate in neurodegenerative diseases and general aging-

induced damage (Yerbury et al., 2016). If this is the case, our study suggests that blocking microglia-specific checkpoints might provide a therapeutic approach to unleash the ability of resident microglia to combat neurodegenerative disorders.

## STAR★METHODS

Detailed methods are provided in the online version of this paper and include the following:

- KEY RESOURCES TABLE
- CONTACT FOR REAGENT AND RESOURCE SHARING
- EXPERIMENTAL MODEL AND SUBJECT DETAILS
  - Animals
  - Paraffin embedded sections of human brains
- METHOD DETAILS
  - Tissue harvesting
  - Single cell Sorting
  - Massively Parallel Single-Cell RNA-seq Library preparation (MARS-seq)
  - Analysis of Single cell RNA-seq data
  - Graph-based clustering analysis
  - Graph projection
  - Single cell clustering Heatmap view
  - Gene enrichment analysis
  - Pseudo-temporal ordering of single cells (along disease progression axis)
  - Immunohistochemistry and histochemistry
  - Single-molecule fluorescent *in situ* hybridization (smFISH)
  - Chromatin immunoprecipitation (iChIP)
  - iChIP analysis
  - Comparing DAM program in AD, ALS and aging
  - Analysis of Trem2 single cell data
- QUANTIFICATION AND STATISTICAL ANALYSIS
- DATA AND SOFTWARE AVAILABILITY

## SUPPLEMENTAL INFORMATION

Supplemental Information includes five figures and seven tables and can be found with this article online at <http://dx.doi.org/10.1016/j.cell.2017.05.018>.

A video abstract is available at <http://dx.doi.org/10.1016/j.cell.2017.05.018#mmc8>.

## AUTHOR CONTRIBUTIONS

H.K.-S. developed experimental protocols, designed, performed, and analyzed experiments, and wrote the manuscript. A.S. designed and performed experiments and performed bioinformatic analysis. A.W. designed and analyzed experiments, developed computational methods, and performed bioinformatic analysis. O.M.-N. designed, performed, and analyzed experiments. R.D.-S. and T.K.U. performed experiments. E.D. performed bioinformatic analysis. K.B., D.L.-A., B.T. contributed to the experiments. S.I. and M.C. contributed to project design. M.S. and I.A. directed the project, designed experiments, interpreted results, and wrote the manuscript.

## ACKNOWLEDGMENTS

We thank Genia Brodsky for help with the artwork. We thank M. Esiri and A. Troen for their help in obtaining human brain sections. This work was funded by NIH grants RF1AG05148501 (M.C.) and 5T32CA009547-30 (T.K.U.). M.S. is

supported by the Advanced European Research Council (232835), by the EU Seventh Framework Program HEALTH-2011 (279017), Israel Science Foundation (ISF)-Legacy-Bio-Med program (1354/15), the Minerva Foundation, and ISF-Neurology (991/16). M.S. holds the Maurice and Ilse Katz Professorial Chair in Neuroimmunology. I.A. is supported by the HHMI International Scholar award, the European Research Council Consolidator Grant (ERC-COG) 724471-HemTree2.0, the Israel Science Foundation (703/15), the Ernest and Bonnie Beutler Research Program of Excellence in Genomic Medicine, the Helen and Martin Kimmel award for innovative investigation, a Minerva Stiftung research grant, the Israeli Ministry of Science, Technology, and Space, the David and Fela Shapell Family Foundation, the NeuroMac DFG/Transregional Collaborative Research Center Grant, and the Abramson Family Center for Young Scientists. I.A. is the incumbent of the Alan and Laraine Fischer Career Development Chair. A patent application has been filed related to this work.

Received: February 6, 2017

Revised: April 10, 2017

Accepted: May 11, 2017

Published: June 8, 2017

## REFERENCES

- Ballard, C., Gauthier, S., Corbett, A., Brayne, C., Aarsland, D., and Jones, E. (2011). Alzheimer's disease. *Lancet* 377, 1019–1031.
- Baruch, K., Rosenzweig, N., Kertser, A., Deczkowska, A., Sharif, A.M., Spinrad, A., Tsitsou-Kampeli, A., Sarel, A., Cahalon, L., and Schwartz, M. (2015). Breaking immune tolerance by targeting Foxp3(+) regulatory T cells mitigates Alzheimer's disease pathology. *Nat. Commun.* 6, 7967.
- Baruch, K., Deczkowska, A., Rosenzweig, N., Tsitsou-Kampeli, A., Sharif, A.M., Matcovitch-Natan, O., Kertser, A., David, E., Amit, I., and Schwartz, M. (2016). PD-1 immune checkpoint blockade reduces pathology and improves memory in mouse models of Alzheimer's disease. *Nat. Med.* 22, 135–137.
- Baum, L., Chen, L., Masliah, E., Chan, Y.S., Ng, H.K., and Pang, C.P. (1999). Lipoprotein lipase mutations and Alzheimer's disease. *Am. J. Med. Genet.* 88, 136–139.
- Bendall, S.C., Davis, K.L., Amir, A.D., Tadmor, M.D., Simonds, E.F., Chen, T.J., Shenfeld, D.K., Nolan, G.P., and Pe'er, D. (2014). Single-cell trajectory detection uncovers progression and regulatory coordination in human B cell development. *Cell* 157, 714–725.
- Butovsky, O., Jedyrchowski, M.P., Cialic, R., Krasemann, S., Murugaiyan, G., Fanek, Z., Greco, D.J., Wu, P.M., Doykan, C.E., Kiner, O., et al. (2015). Targeting miR-155 restores abnormal microglia and attenuates disease in SOD1 mice. *Ann. Neurol.* 77, 75–99.
- Castellano, J.M., Kim, J., Stewart, F.R., Jiang, H., DeMattos, R.B., Patterson, B.W., Fagan, A.M., Morris, J.C., Mawuenyega, K.G., Cruchaga, C., et al. (2011). Human apoE isoforms differentially regulate brain amyloid- $\beta$  peptide clearance. *Sci. Transl. Med.* 3, 89ra57.
- Chakrabarty, P., Li, A., Ceballos-Diaz, C., Eddy, J.A., Funk, C.C., Moore, B., DiNunno, N., Rosario, A.M., Cruz, P.E., Verbeeck, C., et al. (2015). IL-10 alters immunoproteostasis in APP mice, increasing plaque burden and worsening cognitive behavior. *Neuron* 85, 519–533.
- Chiu, I.M., Morimoto, E.T., Goodarzi, H., Liao, J.T., O'Keeffe, S., Phatnani, H.P., Muratet, M., Carroll, M.C., Levy, S., Tavazoie, S., et al. (2013). A neurodegeneration-specific gene-expression signature of acutely isolated microglia from an amyotrophic lateral sclerosis mouse model. *Cell Rep.* 4, 385–401.
- Colonna, M., and Wang, Y. (2016). TREM2 variants: new keys to decipher Alzheimer disease pathogenesis. *Nat. Rev. Neurosci.* 17, 201–207.
- Corder, E.H., Saunders, A.M., Strittmatter, W.J., Schmeichel, D.E., Gaskell, P.C., Small, G.W., Roses, A.D., Haines, J.L., and Pericak-Vance, M.A. (1993). Gene dose of apolipoprotein E type 4 allele and the risk of Alzheimer's disease in late onset families. *Science* 261, 921–923.
- Deardorff, W.J., and Grossberg, G.T. (2017). Targeting neuroinflammation in Alzheimer's disease: evidence for NSAIDs and novel therapeutics. *Expert Rev. Neurother.* 17, 17–32.
- Deng, Q., Ramsköld, D., Reinius, B., and Sandberg, R. (2014). Single-cell RNA-seq reveals dynamic, random monoallelic gene expression in mammalian cells. *Science* 343, 193–196.
- Elowitz, M.B., Levine, A.J., Siggia, E.D., and Swain, P.S. (2002). Stochastic gene expression in a single cell. *Science* 297, 1183–1186.
- Geissmann, F., Gordon, S., Hume, D.A., Mowat, A.M., and Randolph, G.J. (2010). Unravelling mononuclear phagocyte heterogeneity. *Nat. Rev. Immunol.* 10, 453–460.
- Ginhoux, F., and Prinz, M. (2015). Origin of microglia: current concepts and past controversies. *Cold Spring Harb. Perspect. Biol.* 7, a020537.
- Grün, D., Lyubimova, A., Kester, L., Wiebrands, K., Basak, O., Sasaki, N., Clevers, H., and van Oudenaarden, A. (2015). Single-cell messenger RNA sequencing reveals rare intestinal cell types. *Nature* 525, 251–255.
- Guerreiro, R., Wojtas, A., Bras, J., Carrasco, M., Rogeira, E., Majounie, E., Cruchaga, C., Sassi, C., Kauwe, J.S., Younkin, S., et al.; Alzheimer Genetic Analysis Group (2013). TREM2 variants in Alzheimer's disease. *N. Engl. J. Med.* 368, 117–127.
- Guillot-Sestier, M.V., Doty, K.R., Gate, D., Rodriguez, J., Jr., Leung, B.P., Rezai-Zadeh, K., and Town, T. (2015). IL10 deficiency rebalances innate immunity to mitigate Alzheimer-like pathology. *Neuron* 85, 534–548.
- Gurney, M.E., Pu, H., Chiu, A.Y., Dal Canto, M.C., Polchow, C.Y., Alexander, D.D., Caliendo, J., Hentati, A., Kwon, Y.W., Deng, H.X., et al. (1994). Motor neuron degeneration in mice that express a human Cu,Zn superoxide dismutase mutation. *Science* 264, 1772–1775.
- Gury-BenAri, M., Thaiss, C.A., Serafini, N., Winter, D.R., Giladi, A., Lara-Astiaso, D., Levy, M., Salame, T.M., Weiner, A., David, E., et al. (2016). The spectrum and regulatory landscape of intestinal innate lymphoid cells are shaped by the microbiome. *Cell* 166, 1231–1246.
- Hanisch, U.-K., and Kettenmann, H. (2007). Microglia: active sensor and versatile effector cells in the normal and pathologic brain. *Nat. Neurosci.* 10, 1387–1394.
- Hardy, J., and Selkoe, D.J. (2002). The amyloid hypothesis of Alzheimer's disease: progress and problems on the road to therapeutics. *Science* 297, 353–356.
- Haynes, S.E., Hollopeter, G., Yang, G., Kurpius, D., Dailey, M.E., Gan, W.B., and Julius, D. (2006). The P2Y12 receptor regulates microglial activation by extracellular nucleotides. *Nat. Neurosci.* 9, 1512–1519.
- Heppner, F.L., Ransohoff, R.M., and Becher, B. (2015). Immune attack: the role of inflammation in Alzheimer disease. *Nat. Rev. Neurosci.* 16, 358–372.
- Hickman, S.E., and El Khoury, J. (2014). TREM2 and the neuroimmunology of Alzheimer's disease. *Biochem. Pharmacol.* 88, 495–498.
- Hickman, S.E., Kingery, N.D., Ohsumi, T.K., Borowsky, M.L., Wang, L.C., Means, T.K., and El Khoury, J. (2013). The microglial sensome revealed by direct RNA sequencing. *Nat. Neurosci.* 16, 1896–1905.
- Holtzman, D.M., Raj, D.D., Miller, J.A., Schaafsma, W., Yin, Z., Brouwer, N., Wes, P.D., Möller, T., Orre, M., Kamphuis, W., et al. (2015). Induction of a common microglia gene expression signature by aging and neurodegenerative conditions: a co-expression meta-analysis. *Acta Neuropathol. Commun.* 3, 31.
- Holtzman, D.M., Morris, J.C., and Goate, A.M. (2011). Alzheimer's disease: the challenge of the second century. *Sci. Transl. Med.* 3, 77sr1.
- Hume, D.A. (2008). Macrophages as APC and the dendritic cell myth. *J. Immunol.* 181, 5829–5835.
- Itzkovitz, S., Blat, I.C., Jacks, T., Clevers, H., and van Oudenaarden, A. (2012). Optimality in the development of intestinal crypts. *Cell* 148, 608–619.
- Jaitin, D.A., Kenigsberg, E., Keren-Shaul, H., Elefant, N., Paul, F., Zaretsky, I., Mildner, A., Cohen, N., Jung, S., Tanay, A., and Amit, I. (2014). Massively parallel single-cell RNA-seq for marker-free decomposition of tissues into cell types. *Science* 343, 776–779.

- Jaitin, D.A., Weiner, A., Yofe, I., Lara-Astiaso, D., Keren-Shaul, H., David, E., Salame, T.M., Tanay, A., van Oudenaarden, A., and Amit, I. (2016). Dissecting immune circuits by linking CRISPR-pooled screens with single-cell RNA-seq. *Cell* 167, 1883–1896.
- Jay, T.R., Miller, C.M., Cheng, P.J., Graham, L.C., Bemiller, S., Broihier, M.L., Xu, G., Margevicius, D., Karlo, J.C., Sousa, G.L., et al. (2015). TREM2 deficiency eliminates TREM2+ inflammatory macrophages and ameliorates pathology in Alzheimer's disease mouse models. *J. Exp. Med.* 212, 287–295.
- Jonsson, T., Stefansson, H., Steinberg, S., Jónsdóttir, I., Jonsson, P.V., Snædal, J., Björnsson, S., Huttenlocher, J., Levey, A.I., Lah, J.J., et al. (2013). Variant of TREM2 associated with the risk of Alzheimer's disease. *N. Engl. J. Med.* 368, 107–116.
- Junker, J.P., and van Oudenaarden, A. (2014). Every cell is special: genome-wide studies add a new dimension to single-cell biology. *Cell* 157, 8–11.
- Kamphuis, W., Kooijman, L., Schetters, S., Orre, M., and Hol, E.M. (2016). Transcriptional profiling of CD11c-positive microglia accumulating around amyloid plaques in a mouse model for Alzheimer's disease. *Biochim. Biophys. Acta* 1862, 1847–1860.
- Kierdorf, K., and Prinz, M. (2013). Factors regulating microglia activation. *Front. Cell. Neurosci.* 7, 44.
- Kim, D., Langmead, B., and Salzberg, S.L. (2015). HISAT: a fast spliced aligner with low memory requirements. *Nat. Methods* 12, 357–360.
- Kimura, R., and Ohno, M. (2009). Impairments in remote memory stabilization precede hippocampal synaptic and cognitive failures in 5XFAD Alzheimer mouse model. *Neurobiol. Dis.* 33, 229–235.
- Koronyo, Y., Salumbides, B.C., Sheyn, J., Pelissier, L., Li, S., Ljubimov, V., Moyseyev, M., Daley, D., Fuchs, D.T., Pham, M., et al. (2015). Therapeutic effects of glatiramer acetate and grafted CD115<sup>+</sup> monocytes in a mouse model of Alzheimer's disease. *Brain* 138, 2399–2422.
- La Manno, G., Gyllborg, D., Codeluppi, S., Nishimura, K., Salto, C., Zeisel, A., Borm, L.E., Stott, S.R., Toledo, E.M., Villaescusa, J.C., et al. (2016). Molecular diversity of midbrain development in mouse, human, and stem cells. *Cell* 167, 566–580.
- Lai, A.Y., and McLaurin, J. (2012). Clearance of amyloid-β peptides by microglia and macrophages: the issue of what, when and where. *Future Neurol.* 7, 165–176.
- Landel, V., Baranger, K., Virard, I., Loriod, B., Khrestchatsky, M., Rivera, S., Benech, P., and Féron, F. (2014). Temporal gene profiling of the 5XFAD transgenic mouse model highlights the importance of microglial activation in Alzheimer's disease. *Mol. Neurodegener.* 9, 33.
- Lara-Astiaso, D., Weiner, A., Lorenzo-Vivas, E., Zaretsky, I., Jaitin, D.A., David, E., Keren-Shaul, H., Mildner, A., Winter, D., Jung, S., et al. (2014). Immunogenetics. Chromatin state dynamics during blood formation. *Science* 345, 943–949.
- Lauro, C., Catalano, M., Trettel, F., and Limatola, C. (2015). Fractalkine in the nervous system: neuroprotective or neurotoxic molecule? *Ann. N Y Acad. Sci.* 1351, 141–148.
- Lee, S., Varrel, N.H., Konerth, M.E., Xu, G., Cardona, A.E., Ransohoff, R.M., and Lamb, B.T. (2010). CX3CR1 deficiency alters microglial activation and reduces beta-amyloid deposition in two Alzheimer's disease mouse models. *Am. J. Pathol.* 177, 2549–2562.
- Levine, J.H., Simonds, E.F., Bendall, S.C., Davis, K.L., Amir, A.D., Tadmor, M.D., Litvin, O., Fienberg, H.G., Jager, A., Zunder, E.R., et al. (2015). Data-driven phenotypic dissection of AML reveals progenitor-like cells that correlate with prognosis. *Cell* 162, 184–197.
- Louveau, A., Harris, T.H., and Kipnis, J. (2015). Revisiting the Mechanisms of CNS Immune Privilege. *Trends Immunol.* 36, 569–577.
- Ma, J., Jiang, T., Tan, L., and Yu, J.T. (2015). TYROBP in Alzheimer's disease. *Mol. Neurobiol.* 51, 820–826.
- Mass, E., Ballesteros, I., Farlik, M., Halbritter, F., Günther, P., Crozet, L., Jaramillo-Galarza, C.E., Händler, K., Klughammer, J., Kobayashi, Y., et al. (2016). Specification of tissue-resident macrophages during organogenesis. *Science* 353. <http://dx.doi.org/10.1126/science.aaf4238>.
- Matcovitch-Natan, O., Winter, D.R., Giladi, A., Vargas Aguilar, S., Spinrad, A., Sarrazin, S., Ben-Yehuda, H., David, E., Zelada González, F., Perrin, P., et al. (2016). Microglia development follows a stepwise program to regulate brain homeostasis. *Science* 353, aad8670.
- McCombe, P.A., and Henderson, R.D. (2011). The Role of immune and inflammatory mechanisms in ALS. *Curr. Mol. Med.* 11, 246–254.
- Merino, J.J., Muñetón-Gómez, V., Alvarez, M.I., and Toledo-Díaz, A. (2016). Effects of CX3CR1 and fractalkine chemokines in amyloid beta clearance and p-tau accumulation in Alzheimer's disease (AD) rodent models: is fractalkine a systemic biomarker for AD? *Curr. Alzheimer Res.* 13, 403–412.
- Mildner, A., Huang, H., Radke, J., Stenzel, W., and Priller, J. (2017). P2Y12 receptor is expressed on human microglia under physiological conditions throughout development and is sensitive to neuroinflammatory diseases. *Glia* 65, 375–387.
- Mosher, K.I., and Wyss-Coray, T. (2014). Microglial dysfunction in brain aging and Alzheimer's disease. *Biochem. Pharmacol.* 88, 594–604.
- Oakley, H., Cole, S.L., Logan, S., Maus, E., Shao, P., Craft, J., Guillozet-Bongaarts, A., Ohno, M., Disterhoft, J., Van Eldik, L., et al. (2006). Intraneuronal beta-amyloid aggregates, neurodegeneration, and neuron loss in transgenic mice with five familial Alzheimer's disease mutations: potential factors in amyloid plaque formation. *J. Neurosci.* 26, 10129–10140.
- Orre, M., Kamphuis, W., Osborn, L.M., Jansen, A.H., Kooijman, L., Bossers, K., and Hol, E.M. (2014a). Isolation of glia from Alzheimer's mice reveals inflammation and dysfunction. *Neurobiol. Aging* 35, 2746–2760.
- Orre, M., Kamphuis, W., Osborn, L.M., Melief, J., Kooijman, L., Huitinga, I., Klooster, J., Bossers, K., and Hol, E.M. (2014b). Acute isolation and transcriptome characterization of cortical astrocytes and microglia from young and aged mice. *Neurobiol. Aging* 35, 1–14.
- Ostuni, R., Piccolo, V., Barozzi, I., Polletti, S., Termanini, A., Bonifacio, S., Curina, A., Prosperini, E., Ghisletti, S., and Natoli, G. (2013). Latent enhancers activated by stimulation in differentiated cells. *Cell* 152, 157–171.
- Painter, M.M., Atagi, Y., Liu, C.C., Rademakers, R., Xu, H., Fryer, J.D., and Bu, G. (2015). TREM2 in CNS homeostasis and neurodegenerative disease. *Mol. Neurodegener.* 10, 43.
- Paul, F., Arkin, Y., Giladi, A., Jaitin, D.A., Kenigsberg, E., Keren-Shaul, H., Winter, D., Lara-Astiaso, D., Gury, M., Weiner, A., et al. (2015). Transcriptional heterogeneity and lineage commitment in myeloid progenitors. *Cell* 163, 1663–1677.
- Paz-Y-Miño, C.A., García-Cárdenas, J.M., López-Cortés, A., Salazar, C., Serrano, M., and Leone, P.E. (2015). Positive association of the Cathepsin D Ala224Val gene polymorphism with the risk of Alzheimer's disease. *Am. J. Med. Sci.* 350, 296–301.
- Pottier, C., Ravenscroft, T.A., Brown, P.H., Finch, N.A., Baker, M., Parsons, M., Asmann, Y.W., Ren, Y., Christopher, E., Levitch, D., et al. (2016). TYROBP genetic variants in early-onset Alzheimer's disease. *Neurobiol. Aging* 48, 222.e9–222.e5.
- Prinz, M., and Priller, J. (2014). Microglia and brain macrophages in the molecular age: from origin to neuropsychiatric disease. *Nat. Rev. Neurosci.* 15, 300–312.
- Quan, N., and Banks, W.A. (2007). Brain-immune communication pathways. *Brain Behav. Immun.* 21, 727–735.
- Rajamohamedsait, H.B., and Sigurdsson, E.M. (2012). Histological staining of amyloid and pre-amyloid peptides and proteins in mouse tissue. *Methods Mol. Biol.* 849, 411–424.
- Ransohoff, R.M., and Cardona, A.E. (2010). The myeloid cells of the central nervous system parenchyma. *Nature* 468, 253–262.
- Reitz, C., and Mayeux, R. (2014). Alzheimer disease: epidemiology, diagnostic criteria, risk factors and biomarkers. *Biochem. Pharmacol.* 88, 640–651.
- Scacchi, R., Gambina, G., Broggio, E., Moretto, G., Ruggeri, M., and Corbo, R.M. (2004). The H+ allele of the lipoprotein lipase (LPL) HindIII intronic polymorphism and the risk for sporadic late-onset Alzheimer's disease. *Neurosci. Lett.* 367, 177–180.

- Schlegelmilch, T., Henke, K., and Peri, F. (2011). Microglia in the developing brain: from immunity to behaviour. *Curr. Opin. Neurobiol.* 21, 5–10.
- Schwartz, M., and Schechter, R. (2010). Systemic inflammatory cells fight off neurodegenerative disease. *Nat. Rev. Neurol.* 6, 405–410.
- Sierra, A., Beccari, S., Diaz-Aparicio, I., Encinas, J.M., Comeau, S., and Tremblay, M.E. (2014). Surveillance, phagocytosis, and inflammation: how never-resting microglia influence adult hippocampal neurogenesis. *Neural Plast.* 2014, 610343.
- Simard, A.R., Soulet, D., Gowing, G., Julien, J.P., and Rivest, S. (2006). Bone marrow-derived microglia play a critical role in restricting senile plaque formation in Alzheimer's disease. *Neuron* 49, 489–502.
- Song, W., Hooli, B., Mullin, K., Jin, S.C., Cella, M., Ulland, T.K., Wang, Y., Tanzi, R., and Colonna, M. (2017). Alzheimer's disease-associated TREM2 variants exhibit either decreased or increased ligand-dependent activation. *Alzheimers Dement.* 13, 381–387.
- Tejera, D., and Heneka, M.T. (2016). Microglia in Alzheimer's disease: the good, the bad and the ugly. *Curr. Alzheimer Res.* 13, 370–380.
- Thériault, P., ElAli, A., and Rivest, S. (2015). The dynamics of monocytes and microglia in Alzheimer's disease. *Alzheimers Res. Ther.* 7, 41.
- Tremblay, M.E., Stevens, B., Sierra, A., Wake, H., Bessis, A., and Nimmerjahn, A. (2011). The role of microglia in the healthy brain. *J. Neurosci.* 31, 16064–16069.
- Treutlein, B., Brownfield, D.G., Wu, A.R., Neff, N.F., Mantalas, G.L., Espinoza, F.H., Desai, T.J., Krasnow, M.A., and Quake, S.R. (2014). Reconstructing lineage hierarchies of the distal lung epithelium using single-cell RNA-seq. *Nature* 509, 371–375.
- Turnbull, I.R., Gilfillan, S., Cella, M., Aoshi, T., Miller, M., Piccio, L., Hernandez, M., and Colonna, M. (2006). Cutting edge: TREM-2 attenuates macrophage activation. *J. Immunol.* 177, 3520–3524.
- Wang, Y., Cella, M., Mallinson, K., Ulrich, J.D., Young, K.L., Robinette, M.L., Gilfillan, S., Krishnan, G.M., Sudhakar, S., Zinselmeyer, B.H., et al. (2015). TREM2 lipid sensing sustains the microglial response in an Alzheimer's disease model. *Cell* 160, 1061–1071.
- Wang, Y., Ulland, T.K., Ulrich, J.D., Song, W., Tzaferis, J.A., Hole, J.T., Yuan, P., Mahan, T.E., Shi, Y., Gilfillan, S., et al. (2016). TREM2-mediated early microglial response limits diffusion and toxicity of amyloid plaques. *J. Exp. Med.* 213, 667–675.
- Winter, D.R., Jung, S., and Amit, I. (2015). Making the case for chromatin profiling: a new tool to investigate the immune-regulatory landscape. *Nat. Rev. Immunol.* 15, 585–594.
- Yamasaki, R., Lu, H., Butovsky, O., Ohno, N., Rietsch, A.M., Cialic, R., Wu, P.M., Doykan, C.E., Lin, J., Cotleur, A.C., et al. (2014). Differential roles of microglia and monocytes in the inflamed central nervous system. *J. Exp. Med.* 217, 1533–1549.
- Yerbury, J.J., Ooi, L., Dillin, A., Saunders, D.N., Hatters, D.M., Beart, P.M., Cashman, N.R., Wilson, M.R., and Ecroyd, H. (2016). Walking the tightrope: proteostasis and neurodegenerative disease. *J. Neurochem.* 137, 489–505.
- Yuan, P., Condello, C., Keene, C.D., Wang, Y., Bird, T.D., Paul, S.M., Luo, W., Colonna, M., Baddeley, D., and Grutzendler, J. (2016). TREM2 haploinsufficiency in mice and humans impairs the microglia barrier function leading to decreased amyloid compaction and severe axonal dystrophy. *Neuron* 90, 724–739.
- Zeisel, A., Muñoz-Manchado, A.B., Codeluppi, S., Lönnberg, P., La Manno, G., Juréus, A., Marques, S., Munguba, H., He, L., Betsholtz, C., et al. (2015). Brain structure. Cell types in the mouse cortex and hippocampus revealed by single-cell RNA-seq. *Science* 347, 1138–1142.
- Ziv, Y., Ron, N., Butovsky, O., Landa, G., Sudai, E., Greenberg, N., Cohen, H., Kipnis, J., and Schwartz, M. (2006). Immune cells contribute to the maintenance of neurogenesis and spatial learning abilities in adulthood. *Nat. Neurosci.* 9, 268–275.

## STAR★METHODS

## KEY RESOURCES TABLE

REAGENT or RESOURCE	SOURCE	IDENTIFIER
<b>Antibodies</b>		
Mouse anti-CD45 Brilliant violet 421 (clone 30-F11)	Biolegend	103134
Mouse anti-CD11b APC (clone M1/70)	eBioscience	17-0112-82
Mouse anti-CD11b FITC (clone M1/70)	Biolegend	101206
Mouse anti-CD11c biotin (clone N418)	Biolegend	117304
Streptavidin APC/Cy7	Biolegend	405208
Mouse anti-Ly-6G (Gr-1) PerCP-Cy5.5 (clone RB6-8C5)	eBioscience	45-5931-80
Mouse anti-CD11c (clone AP-MAB0806)	Novus	NB110-97871
Mouse Anti-Lipoprotein lipase antibody (clone LPL.A4)	Abcam	ab21356
Rabbit anti-Iba1	Wako	019-19741
Goat anti-Iba1	Abcam	ab5076
Anti b-amyloid (clone 1-16)	Biolegend	803001
Mouse anti-Timp2 (clone 3A4)	Abcam	ab1828
Cy2 donkey anti-mouse	Jackson	715-225-151
Cy2 donkey anti-rabbit	Jackson	711-225-152
Cy3 donkey anti-mouse	Jackson	715-165-151
Cy3 donkey anti-rabbit	Jackson	711-165-152
Cy5 donkey anti-mouse	Jackson	715-175-151
Alexa Fluor-647 Donkey anti-rabbit (similar to cy5)	Jackson	711-605-152
Cy2 streptavidin	Jackson	016-220-084
Cy3 streptavidin	Jackson	016-160-084
Anti-Histone H3	Abcam	ab1791
<b>Biological Samples</b>		
Human brain sections of postmortem Alzheimer's disease and non-CNS-disease aged matched individuals	Oxford Brain Bank	<a href="http://www.hra.nhs.uk/news/research-summaries/the-oxford-brain-bank/">http://www.hra.nhs.uk/news/research-summaries/the-oxford-brain-bank/</a>
<b>Chemicals, Peptides, and Recombinant Proteins</b>		
Hoechst 33342 (used for nuclear staining)	Invitrogen	H1399
Dynabeads protein G	Invitrogen	10004D
Thioflavine S	Sigma-Aldrich	T1892
<b>Deposited Data</b>		
Raw data files for single-cell RNA-seq	NCBI Gene Expression Omnibus	GSE98969
Raw data files for iChIP	NCBI Gene Expression Omnibus	GSE98970
<b>Experimental Models: Organisms/Strains</b>		
Mouse: 5XFAD Tg6799	The Jackson Laboratory	34840-JAX
Mouse: C57BL/6 WT	Harlan	N/A
Mouse: SOD1-G93A	The Jackson Laboratory	002726
Mouse:Trem2 <sup>-/-</sup>	Generated in the Laboratory of Dr. Marco Colonna	N/A
<b>Oligonucleotides</b>		
Lpl FISH probes:	Stellaris FISH Probes	SMF-1082-5
gaacagttacaaggggcaga		
tcaacccttaaagggggg		
aaggcggtcaaactctggag		
tgtctgagaaatcttccc		

(Continued on next page)

***Continued***

REAGENT or RESOURCE	SOURCE	IDENTIFIER
ccttagggcaaatttgcitt		
gagtctgctaattccaggaaat		
ggttgaagtggcgagtttagac		
cacccaactctatacacattc		
cactggataatgttgctgggg		
atgaatctggccacatcatt		
gtcttaggggttagtttaact		
ttcttattggtcagacttcc		
tgcatactcaaaggtaggcc		
caataactcgaccaggtagac		
aatgtcaacatgcctactg		
tctctgcaatcacacggatg		
ccagattgttacagcgattc		
ctgacaccttgtatcata		
tggAACACTTGTAGGGCAT		
gtgccgtacagagaaatc		
cagggtgaagggatgttct		
cacccctcgtaaatcaaga		
cttcatcatgagcagtttc		
ctgaagttaggagtgcctt		
aaacactgctgagtc		
ctcaggaaaacccacttca		
gttagccaccgttaatatt		
ggtcacatgtggagtctt		
aaatggacactgacttatgc		
aaaggcccagggtttcaatc		
atgtttcaactgctttgc		
aagggtcaggacttcatgag		
gacttgtacttgtgtgtgt		
gtcttaggtttgtatctctg		
tggcggagatgagtc		
gcagttacaaggcatccata		
attacagtggaggc		
atgacgactacactgtggg		
atattccagtatacccttg		
attacataggcacaaccagc		
tgaaatcggtcaccc		
tagcaataatggggatgc		
caagcattttcacataccca		
gcaccacaaatctatactgc		
atcatggatggagacggaca		
gttaagtggctcagtgaga		
gcctattttatgtactgt		
taccattttcacacagg		
Csf1 FISH probes:	Stellaris FISH Probes	Custom (Hybridized in lab)
tttatggaaatcaccc		
gaggccaaacttcacttcc		
caatcatgtggctacagt		

(Continued on next page)

***Continued***

REAGENT or RESOURCE	SOURCE	IDENTIFIER
ttgactgtcgatcaactgct		
gccttcatttaggttagcaaac		
attgggggttgtgtctttaa		
aggttattggagagtccgt		
tggaaagttcggacacaggc		
gtcctttcaaggagattct		
gttggtcagtttggtaa		
gtacaggcagttgaatcag		
tctgtcctctgagaatcatc		
tttggttgctctgttgactc		
gcagaaggatgagggtgtga		
tgcccagtgaagattcaaga		
cagaagcttcttaggacc		
tcaaaaatccctcaactagcc		
gaatggagatgctgagaggg		
tgttatatccactggctttt		
agtattattctgtgtctggc		
gcttttggaaagcagtaact		
cctgtgtcagtcaaaggaaat		
agggtggaaagacagactcagg		
tccactttagaaacaggagg		
agaatccaatgtctgagggt		
gaatcccttatactggca		
tgtctccctccataaagaga		
agggtgaggatggaaagacc		
caggggccacaataaaatagt		
ctggtttgagggggaggaag		
ctcttcggaaacaggc		
tttatgccttacggaaagt		
aagctgtcaacacaagcagc		
tatcagcagggcacttaa		
agaacattcggacggatggt		
ctcctggaaatgtcaaagt		
ttcaagaccattctcatc		
aatttcaagcttagggtg		
gaggggctagagtatagaga		
agtatggtaggtgagactgg		
ctctaaacctggcttgctt		
ggggactcagcagcataaaag		
gcctgaaagattttgaccc		
tgttgaggttacagaccac		
ccacaagaaggctccagt		
agtctgttaaccagaaggct		
ctccaaagggtggatttgagg		
tcacagtttgaggcagt		
Cx3cr1 FISH probes:	Stellaris FISH Probes	Custom (Hybridized in lab)
agcagatggaaagggaactt		
aaggaggtggacatggtgag		

(Continued on next page)

***Continued***

REAGENT or RESOURCE	SOURCE	IDENTIFIER
attctctagatccaggtagcg		
ttccaaaggccacaatgtcg		
gcgtagaagacggacaggaa		
accagaccgaacgtgaagac		
tcaggaggttagatgtcagtg		
caaagagcaggcgctcaag		
atggctgatgaggtagtgag		
agaagaaggcagtgcgtgagc		
agaatatgcggccaaagaag		
tcgatgtgtatgcgggtat		
agactaatggtgacaccgtg		
tgtccttctttgtgaac		
aggatgtgacttccgagg		
catgataagaaggcagggg		
ggatgtgcggaaatgtggaa		
cttgcgttcttcggggaaa		
agaacttggaggtctccagg		
catgtcacaactggggaa		
ggcgttagataaagggttga		
ccagggtatcttcgttgcactt		
tcgcgttgcgtgtggaa		
agaactctgggttcgttgc		
agcggcaggaaatctgtat		
gcagtaagagatactgttgt		
attttgcaccgttaagcc		
aaaccctttgttaattgcac		
catgtatgtcaaccaggac		
cagtctggggacttagttgt		
gatctgaagggtcagagaggg		
agaacctggatgtgtca		
aatcagagatgtgtgtct		
tgttcccttagaaatccaat		
taacaccacccatgtcaagga		
ttaggtatcccttctatttc		
agttctgtgtcagatgt		
gaatgagctccatgttgc		
gctagcaacagatactgtca		
gtgagcgttaacccaaattc		
gccttggattgttgcattgtat		
gttagaactgcatttatct		
aatggggaggcgtggag		
catggctttcttatttctt		
tatgaatcgtcccttact		
tgtgcaagcaacagatgttg		
gaatggatgttgcggccaca		
atgctaaagtccgtgttag		
atttctcagaggcagggtaa		

(Continued on next page)

**Continued**

REAGENT or RESOURCE	SOURCE	IDENTIFIER
ggatgcgttaggaataggc		
gacatggaaatggcttgta		
gacattcttggtggctacatc		
gagaccggaggcagtgaatg		
ctttcaatgttaagcctgcaa		
tttttgactacactgtcct		
accaacacaggAACAGGGAG		
gctgggagagactctgaaa		
aggagatatcagacatgccg		
tatgactcgatctgtcgtc		
atagacacactctaggcacg		
Software and Algorithms		
MATLAB R2016a software	MathWorks	<a href="http://www.mathworks.com/">http://www.mathworks.com/</a>
HISAT	Kim et al., 2015	<a href="https://github.com/infphilo/hisat">https://github.com/infphilo/hisat</a>
PhenoGraph	Levine et al., 2015	N/A
Other		
MARS-seq reagents	Jaitin et al., 2014	N/A
iChIP reagents	Lara-Astiaso et al., 2014	N/A

**CONTACT FOR REAGENT AND RESOURCE SHARING**

Further information and requests for reagents should be directed to and will be fulfilled by Lead Contact Ido Amit ([ido.amit@weizmann.ac.il](mailto:ido.amit@weizmann.ac.il)).

**EXPERIMENTAL MODEL AND SUBJECT DETAILS****Animals**

Heterozygous 5XFAD transgenic mice (on a C57/BL6-SJL background) that overexpress familial AD mutant forms of human APP (the Swedish mutation, K670N/M671L; the Florida mutation, I716V; and the London mutation, V717I) and PS1 (M146L/L286V) transgenes under the transcriptional control of the neuron-specific mouse Thy-1 promoter ([Oakley et al., 2006](#)) (5XFAD line Tg6799; The Jackson Laboratory), and male Heterozygous mSOD1 G93A mice on a C57BL/6J background, were taken throughout adulthood in different time points as indicated in the text. Mice were bred and maintained by the animal breeding center of the Weizmann Institute of Science. All experiments detailed herein complied with the regulations formulated by the Institutional Animal Care and Use Committee (IACUC) of the Weizmann Institute of Science. For the Trem2 experiments, Trem2<sup>-/-</sup> mice were generated as previously described ([Turnbull et al., 2006](#)); 5XFAD mice were purchased from the Jackson Laboratory (MMRRC) and crossed to Trem2<sup>-/-</sup> mice to generate Trem2<sup>+/-</sup>5XFAD and Trem2<sup>-/-</sup>5XFAD mice. These mice were bred and housed in the Washington University animal house.

**Paraffin embedded sections of human brains**

Human brain sections of postmortem Alzheimer's disease and non-CNS-disease aged matched individuals were obtained from the Oxford Brain Bank (formerly known as the Thomas Willis Oxford Brain Collection (TWDBC)) with appropriate consent and Ethics Committee approval (TW220). The experiments involving these sections were approved by the Weizmann Institute of Science Bioethics Committee.

**METHOD DETAILS****Tissue harvesting**

Mice were transcardially perfused with PBS before tissue extraction. Either whole brains, spinal cords, or specific parts of the brain (cortex or cerebellum), not excluding meninges and choroid plexus, were collected, as indicated in the figure legends. Single-cell suspensions of tissues for all mice, excluding the Trem2 experiment, were achieved using software-controlled sealed homogenization system (Dispomix; <http://www.biocellisolation.com>) in PBS, followed by density gradient separation; Pellet was mixed with 40% percoll and centrifuged in 800G for 20 min at 12°C. Brains of Trem2 mice were processed as previously published ([Wang et al., 2015](#)).

Supernatant was discarded and pellet was taken further for antibody staining, as described below. Before staining, samples were blocked with Fc-block CD16/32 (BD Biosciences, San Jose, CA).

### Single cell Sorting

Cell populations were sorted with SORP-aria (BD Biosciences, San Jose, CA). Prior to sorting, all samples were filtered through a 70- $\mu\text{m}$  nylon mesh. For the sorting of whole immune cell populations, samples were gated for CD45<sup>+</sup> (Brilliant-violet-421, 1:150, 30-F11, biolegend Inc. San Diego, CA), after exclusion of doublets. For the isolation of CD11c positive microglia, samples were gated positive for CD45, CD11b (APC CD11b, 1:100, M1/70, eBioscience or FITC CD11b, 1:100, M1/70, Biolegend Inc), and CD11c (Biotin CD11c, 1:100, N418, Biolegend Inc, followed by APC/Cy7 Streptavidin, 1:100, Biolegend Inc.), while excluding Gr-1 positive cells (PerCP Cy5.5, 1:100, RB6-8C5, eBioscience) and doublets. Isolated cells were single cell sorted into 384-well cell capture plates containing 2  $\mu\text{L}$  of lysis solution and barcoded poly(T) reverse-transcription (RT) primers for single-cell RNA-seq (Jaitin et al., 2014). Four empty wells were kept in each 384-well plate as a no-cell control during data analysis. Immediately after sorting, each plate was spun down to ensure cell immersion into the lysis solution, snap frozen on dry ice, and stored at -80°C until processed.

To record marker level of each single cell, the FACS Diva 7 “index sorting” function was activated during single cell sorting. Following the sequencing and analysis of the single cells, each surface marker was linked to the genome-wide expression profile. This methodology was used to optimize the gating strategy.

### Massively Parallel Single-Cell RNA-seq Library preparation (MARS-seq)

Single-cell libraries were prepared as previously described (Jaitin et al., 2014). In brief, mRNA from cell sorted into cell capture plates are barcoded and converted into cDNA and pooled using an automated pipeline. The pooled sample is then linearly amplified by T7 in vitro transcription, and the resulting RNA is fragmented and converted into a sequencing-ready library by tagging the samples with pool barcodes and illumina sequences during ligation, RT, and PCR. Each pool of cells was tested for library quality and concentration is assessed as described earlier (Jaitin et al., 2014).

### Analysis of Single cell RNA-seq data

MARS-seq libraries, pooled at equimolar concentrations, were sequenced using an Illumina NextSeq 500 sequencer, at a sequencing depth of 50K-100K reads per cell. Reads are condensed into original molecules by counting same unique molecular tags (UMI). We used statistics on empty-well spurious UMI detection to ensure that the batches we used for analysis showed a low level of cross-single-cell contamination (less than 3%).

MARS-seq reads were processed as previously described (Gury-BenAri et al., 2016). Mapping of reads was done using HISAT (version 0.1.6) (Kim et al., 2015); reads with multiple mapping positions were excluded. Reads were associated with genes if they were mapped to an exon, using the UCSC genome browser for reference. Exons of different genes that shared genomic position on the same strand were considered a single gene with a concatenated gene symbol. Cells with less than 500 UMIs were discarded from the analysis. Genes with mean expression smaller than 0.005 UMIs/cell or with above average expression and low coefficient of variance (< 1.2) were also discarded. After filtering, cells contained a median of 2,373 unique molecules with 1,179 median genes per cell.

### Graph-based clustering analysis

In order to assign cells to homogeneous clusters we used the PhenoGraph clustering algorithm (Levine et al., 2015). Low-level processing of MARS-seq reads results in a matrix  $U$  with  $n$  rows and  $m$  columns, where rows represent genes and columns represent cells. Entry  $U_{ij}$  contains the number of unique molecular identifiers (UMIs) from gene  $i$  that were found in cell  $j$ . PhenoGraph first builds a  $k$ -Nearest Neighbors (kNN) graph using the Euclidean distance ( $k = 30$ ) and then refines this graph with the Jaccard similarity coefficient, where the edge weight between each two nodes is the number of neighbors they share divided by the total number of neighbors they have (Levine et al., 2015). As input for PhenoGraph we first applied PCA of the expression matrix keeping the first 40 components. To partition the graph into modules/communities PhenoGraph uses the Louvain Method (Levine et al., 2015). p values for differential expression analysis between different clusters were calculated using the Mann-Whitney U test (MATLAB R2016a *ranksum* function). Clusters annotation was done manually based on the expression of a large number of hallmark genes, for example, CD3 for T cells, S100A6 for granulocytes and Hexb, Cst3 and Cx3cr1 for microglia.

### Graph projection

Graph is visualized in two dimensions using ‘force-directed layout’ (MATLAB R2016a *graph plot* function). Using attractive forces between adjacent nodes and repulsive forces between distant nodes.

### Single cell clustering Heatmap view

For heatmap visualization of single cell clusters we selected the variable genes (rows) using a chi-square based assay. Cells were grouped according to their assignment to clusters, and the number of UMIs per gene in each cluster was compared against the expected number. Genes with p value passing a threshold of 1e-3 after a Bonferroni correction were selected for visualization. Values were log transformed and normalized to have mean expression of 1, genes were ordered using hierarchical clustering with correlation distance.

## Gene enrichment analysis

Gene enrichment was done using Metascape (<http://metascape.org/>) online tool with default parameters.

## Pseudo-temporal ordering of single cells (along disease progression axis)

To obtain pseudo-temporal ordering of the cells along the transition from homeostatic microglia into DAM we used a similar approach to Wanderlust (Bendall et al., 2014). Cells were represented as nodes in a k-nearest neighbor graph. We selected a representative homeostatic microglia cell (from the homeostatic microglia cluster) and a representative DAM cell as waypoints. For each cell we calculated the shortest path to each of the waypoints and ordered the cells according to their distance. The final trajectory is an average over all graph trajectories. One-dimensional PCA trajectory resulted in a very similar path, suggesting that the majority of the variability inherent in our dataset can be represented by a single principal component.

To estimate the pseudo-time transition point for each gene we sorted the cells according to their temporal ordering. For each gene, we fitted a generalized logistic function (Richards' curve) to the one dimensional vector of UMI counts using nonlinear optimization algorithm (MATLAB R2016a *fmincon* function). Genes were ordered according to time to half maximal response ( $t_{1/2}$ ).

## Immunohistochemistry and histochemistry

Immunohistochemistry and histological staining was performed on human and mouse brain sections. Mice were perfused with PBS prior to brain tissue fixation, followed by tissue processing to form 30  $\mu$ m thick floating sections. Human hippocampal paraffin embedded sections were 10  $\mu$ m thick. Histological staining for A $\beta$  was done using Thioflavin S (ThioS). The following primary antibodies were used: Armenian Hamster anti-CD11c (1:50; Novus, Littleton, CO), rabbit anti-IBA-1 (1:100, Wako, Richmond, VA), goat anti-IBA1 (1:200, Abcam, Cambridge, MA), mouse anti-LPL (1:50, Abcam, Cambridge, MA), mouse anti-A $\beta$  1-16 (1:200, Biolegend, San Diego, CA), mouse anti-TIMP2 (1:25, Abcam, Cambridge, MA). Secondary antibodies were Cy2/Cy3/Cy5 donkey anti-rabbit/mouse antibodies (1:150; Jackson ImmunoResearch, West Grove, PA) or biotin-SP-conjugated goat anti-Armenian Hamster following cy2/cy3 conjugated streptavidin (1:150; Jackson ImmunoResearch, West Grove, PA). The slides were exposed to Hoechst nuclear staining (1:4000; Invitrogen Probes, Carlsbad, CA) for 30 s, prior to their sealing. Staining with secondary antibody alone was used as a negative control. Microscopic analysis was performed using confocal microscopy (Zeiss, LSM880). For quantification of IBA-1+ CD11c+ microglia from cortical slices, IBA-1+ and IBA-1+ CD11c+ cells were counted manually using ImageJ (805 IBA-1+ cells in AD and 139 IBA-1+ in the WT). Quantification of IBA-1+ LPL+ ThioS+ microglia was performed by acquisition of z stacks to allow a 3D analysis using the IMARIS software. 109 IBA-1+ mouse cells were counted in A $\beta$  proximal regions and 102 IBA-1+ cells in A $\beta$  distal regions. 110 IBA-1+ human cells were counted in each region.

## Single-molecule fluorescent in situ hybridization (smFISH)

5XFAD and WT 6-month old female mice were perfused with PBS. Brain tissues harvested and fixed in 4% paraformaldehyde for 3 hr; incubated overnight with 30% sucrose in 4% paraformaldehyde and then embedded in OCT. 6-10  $\mu$ m cryosections were used for hybridization. Probe libraries were designed and constructed as previously described (Itzkovitz et al., 2012). Single molecule FISH probe libraries consisted of 48 probes of length 20 bps. Lpl, Cx3cr1, and Csf1 probes were coupled to cy5 or alexa594. Hybridizations were performed overnight in 30°C. DAPI dye for nuclear staining was added during the washes. To detect amyloid plaques,  $\alpha$ A $\beta$  immunohistochemistry staining was performed simultaneously with the hybridization. Images were taken with a Nikon Ti-E inverted fluorescence microscope equipped with a x60 and  $\times$  100 oil-immersion objective and a Photometrics Pixis 1024 CCD camera using MetaMorph software (Molecular Devices, Downington, PA). Quantification was done manually and calculated according to proximity to the A $\beta$  (AD-A $\beta$  proximal and AD-A $\beta$  distal). AD-A $\beta$  proximal were considered areas that had more than one plaque with a diameter over 35  $\mu$ m in a field of x60 magnification. smFISH molecules were counted only within the DAPI staining of the cell; a cell was considered Cx3cr1-positive if it had more than 4 Cx3cr1 molecules over 20 0.3  $\mu$ m Z stacks. The number of molecules of Lpl, Csf1 was counted over 20 or 21 0.3  $\mu$ m Z stacks and normalized to 20 Z stacks. The p values were achieved using Mann-Whitney U test (MATLAB R2016a *ranksum* function).

## Chromatin immunoprecipitation (iChIP)

iChIP was prepared as previously described (Lara-Astiaso et al., 2014). Briefly, for chromatin analysis, cells were cross-linked for 8 min in 1% formaldehyde and quenched for 5 min in 0.125 M glycine prior to sorting. Cells were sorted using the described sorting strategy for CD11c positive microglia. Brains from five 5XFAD mice at ages 5.8-7.4 months were combined for the iChIP experiment. WT control was aged matched. Sorted cells were lysed in 0.5% SDS and sheared with the NGS Bioruptor Sonicator (Diagenode). Sheared chromatin was immobilized on 15  $\mu$ L Dynabeads Protein G (Invitrogen) with 1.3  $\mu$ g of anti-H3 antibody (Abcam). Magnetized chromatin was then washed with 10mM Tris-HCl supplemented with 1X PI. Chromatin was end repaired, dA-tailed and ligated with sequencing adapters containing Illumina P5 and P7 sequences. Indexed chromatin was pooled and incubated with 2.5  $\mu$ g H3K4me2 antibody (ab32356) at 4°C for 3 hr and for an additional hour with Protein G magnetic beads (Invitrogen). Magnetized chromatin was washed and reverse cross-linked. DNA was subsequently purified with 1.65X SPRI and amplified by PCR with 0.5  $\mu$ M of forward and reverse primers containing Illumina P5-rd1 and P7-rd2 sequences. Library concentration was measured with a Qubit fluorometer and mean molecule size was determined by TapeStation (Agilent). DNA libraries were sequenced on an Illumina NextSeq 500 with an average of over 10 million aligned reads per replicate.

### iChIP analysis

Reads were aligned to the mouse reference genome (mm9, NCBI 37) using Bowtie2 aligner version 2.2.5 with default parameters. The Picard tool MarkDuplicates from the Broad Institute (<http://broadinstitute.github.io/picard/>) was used to remove PCR duplicates. For scatterplot, the read density (number of reads in 10 million total reads per 1000 bp) was calculated using a sliding window across the entire genome of with 500bp overlap. The region intensity was given in log-base2 of the normalized density ( $\log_2(x+1)$ ).

### Comparing DAM program in AD, ALS and aging

To compare the DAM expression profile between various neurodegenerative conditions we used correlation between the average expression profiles of the DAM cluster in each condition including all genes with at least 0.1 molecules per cell in any condition ( $r > 0.9$  for pairwise correlations). In addition, we have searched for differential genes using the non-parametric Mann–Whitney U test comparing the two clusters and did not find significant changes of the DAM program between the different conditions.

### Analysis of Trem2 single cell data

Trem2 experiment (related to Figure 5) was performed using a different cell processing protocol (Wang et al., 2015); we therefore detected an increase in the expression of stress related genes, such as Fos, Jun, Junb, Klf6, as well as some inflammatory genes, such as Nfkbbz, Tnf, Tnfaip3. This stress / inflammation pattern was not consistent between WT or AD mice and was observed in both samples in different levels, stronger in the WT Trem2<sup>+/+</sup> sample. As these genes were not expressed in our previous datasets, we assume they are an artifact of the tissue processing protocol. To exclude this potential source of variability we performed the Trem2 analysis using the same gene sets used in the time course experiment. The stress / inflammation related genes are indicated in red in Table S7.

### QUANTIFICATION AND STATISTICAL ANALYSIS

p values for differential expression analysis between different clusters were calculated using the Mann-Whitney U test (MATLAB R2016a *ranksum* function), comparing molecular count in single cells from each group using a non-parametric statistical test.

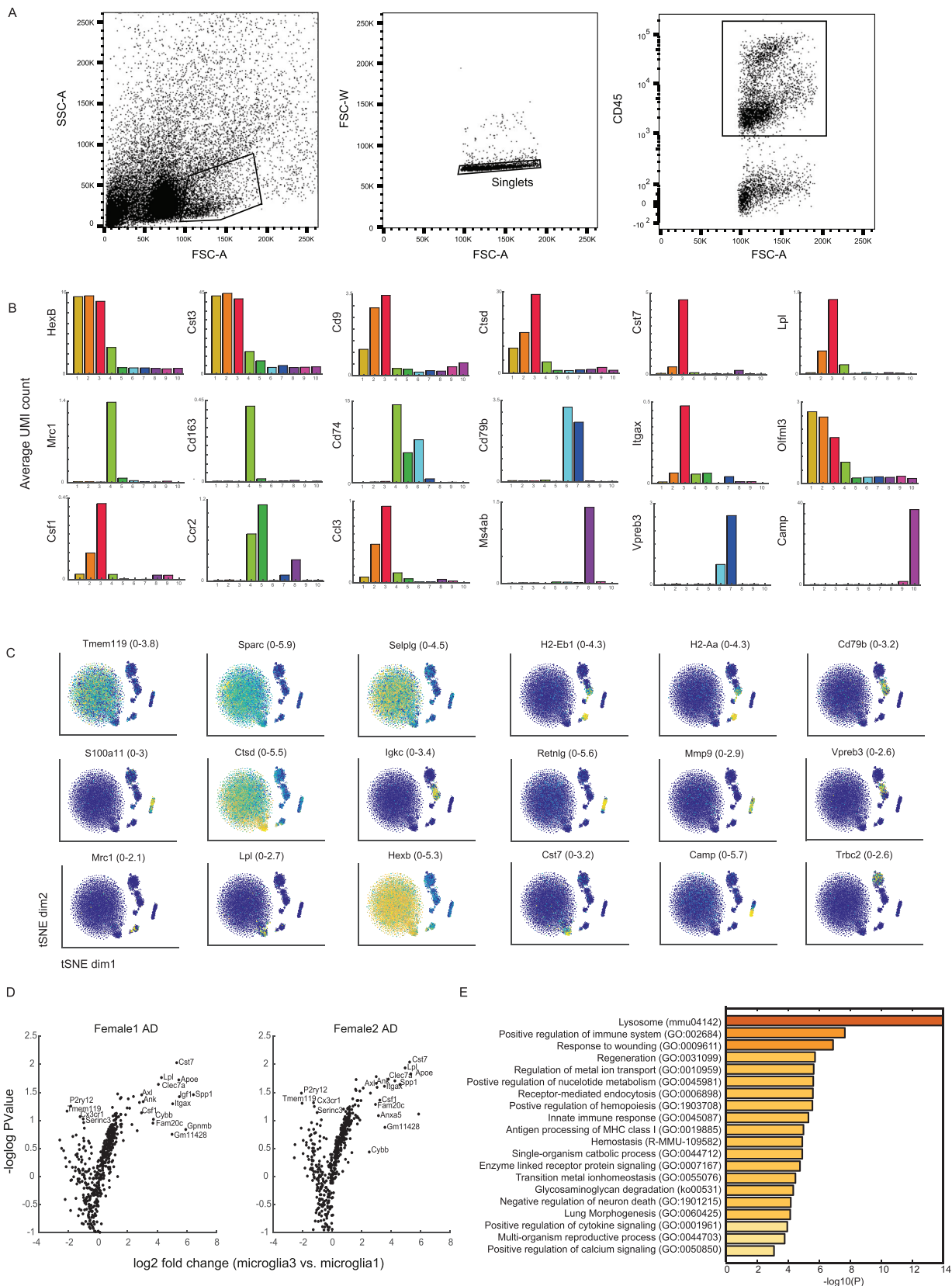
Quantification of immunofluorescence imaging (over 900 cells) as well as single molecule FISH analysis (over 100 cells) was done using the Mann-Whitney U test (MATLAB R2016a *ranksum* function).

### DATA AND SOFTWARE AVAILABILITY

The accession number for the sequencing data reported in this paper is GEO: GSE98971. This parent directory includes the following datasets: GEO: GSE98969 (single cell RNA-seq) and GEO: GSE98970 (iChIP).

# Supplemental Figures

Cell

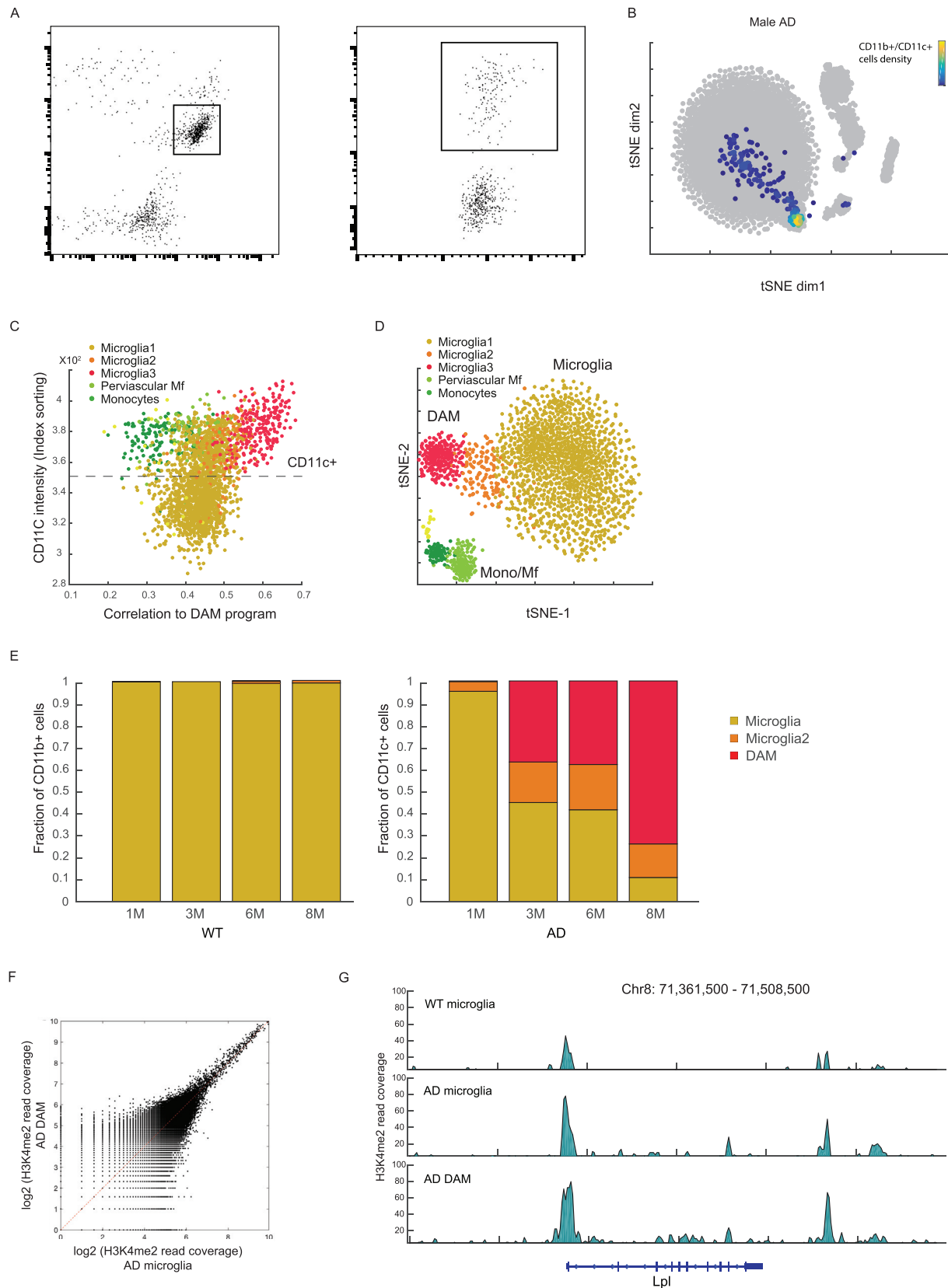


(legend on next page)

---

**Figure S1. Clustering of Immune Cells in the Brain of an AD Mouse Model, Related to Figure 1**

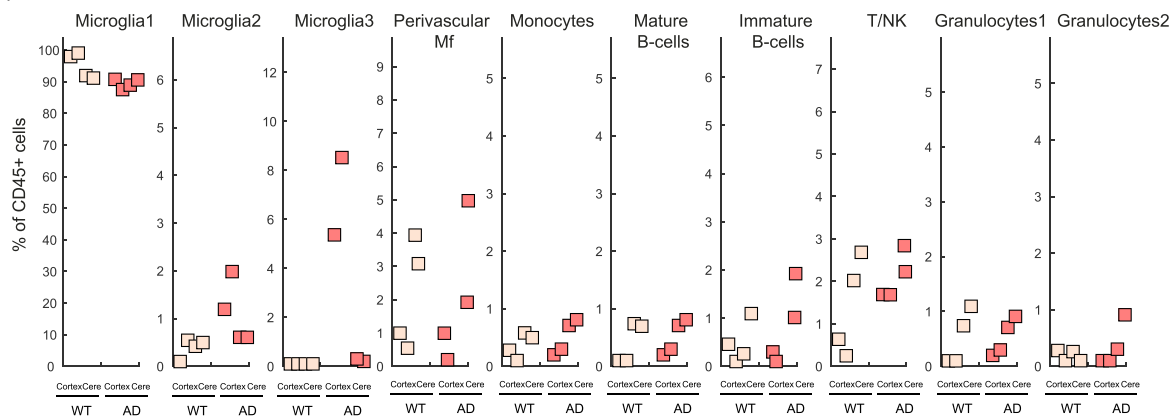
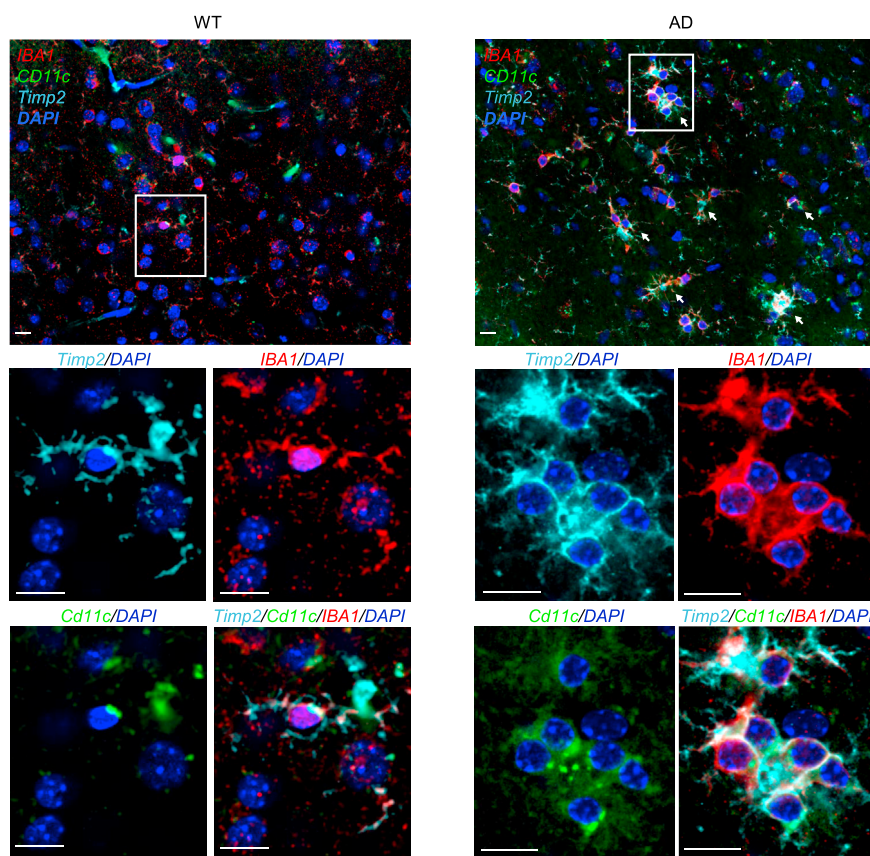
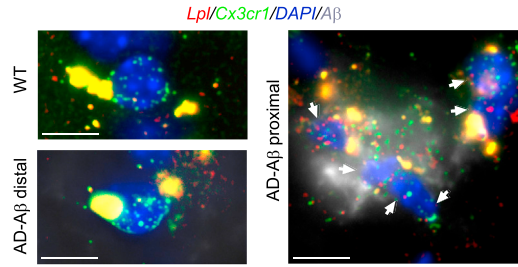
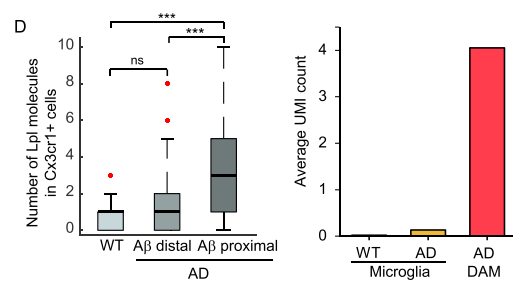
(A) FACS gating strategy for isolating immune cells (CD45+) from whole brains of AD and WT mice. (B) Bar plots showing mean expression (UMI count) of selected genes across clusters I-X (colored as in [Figure 1B](#)) analyzed from the immune cells in the brains of WT and Tg-AD (AD) mice. (C) Projection of selected genes onto the t-SNE plot depicting the ten immune clusters in WT and AD brains (corresponding to [Figure 1D](#)). Number for each gene represents the max expression level ( $\log_2$  UMI counts) depicted by a color bar (similar to [Figure 2D](#)). (D) Volcano plot showing the fold change of genes ( $\log_2$  scale) in individual animals (females) between DAM (microglia3) to regular microglia (microglia1) from the AD brain (x axis) and their significance (y axis, -log<sub>10</sub> scale). p values were determined by Mann-Whitney U-test with FDR correction. (E) Gene Ontology (GO) analysis showing enrichment of GO terms in DAM associated genes.



(legend on next page)

**Figure S2. Analysis of DAM in AD, Related to Figure 2**

(A) FACS gating strategy using the CD11c positive cells for enriching the DAM population in AD brain. (B) Heatmap showing projection of CD11c+ microglia from 6-month old AD mice onto the corresponding CD45+ selection. (C) Scatterplot showing the correlation to the average DAM transcription program (x axis) and index-sorting intensities of CD11c (y axis). Cells are colored based on cluster association as determined in Figure 1D. All DAM cells (red) show high levels ( $> 3.5E^2$ ) of CD11c but not all CD11c cells are DAM. (D) tSNE plot of CD11b+ cells from both WT and AD mouse. (E) Distribution of microglia, intermediate state and DAM in cells sorted at the four time points taken, for WT (CD11b+) and AD (CD11b+CD11c+) mice. (F) Scatterplot showing a 2Kb sliding window read coverage (log2) of H3K4me2 in microglia isolated from brains of AD model (x axis) versus DAM (y axis). AD mice were 6.7-month old on average. See the [STAR Methods](#) for details. (G) Normalized profiles of H3K4me2 signals in 150 kilobase (kb) regions in the Lpl gene analyzed in microglia from brains of 6 months WT mouse (WT microglia), microglia from AD mouse (AD microglia) and DAM from AD mouse (AD DAM).

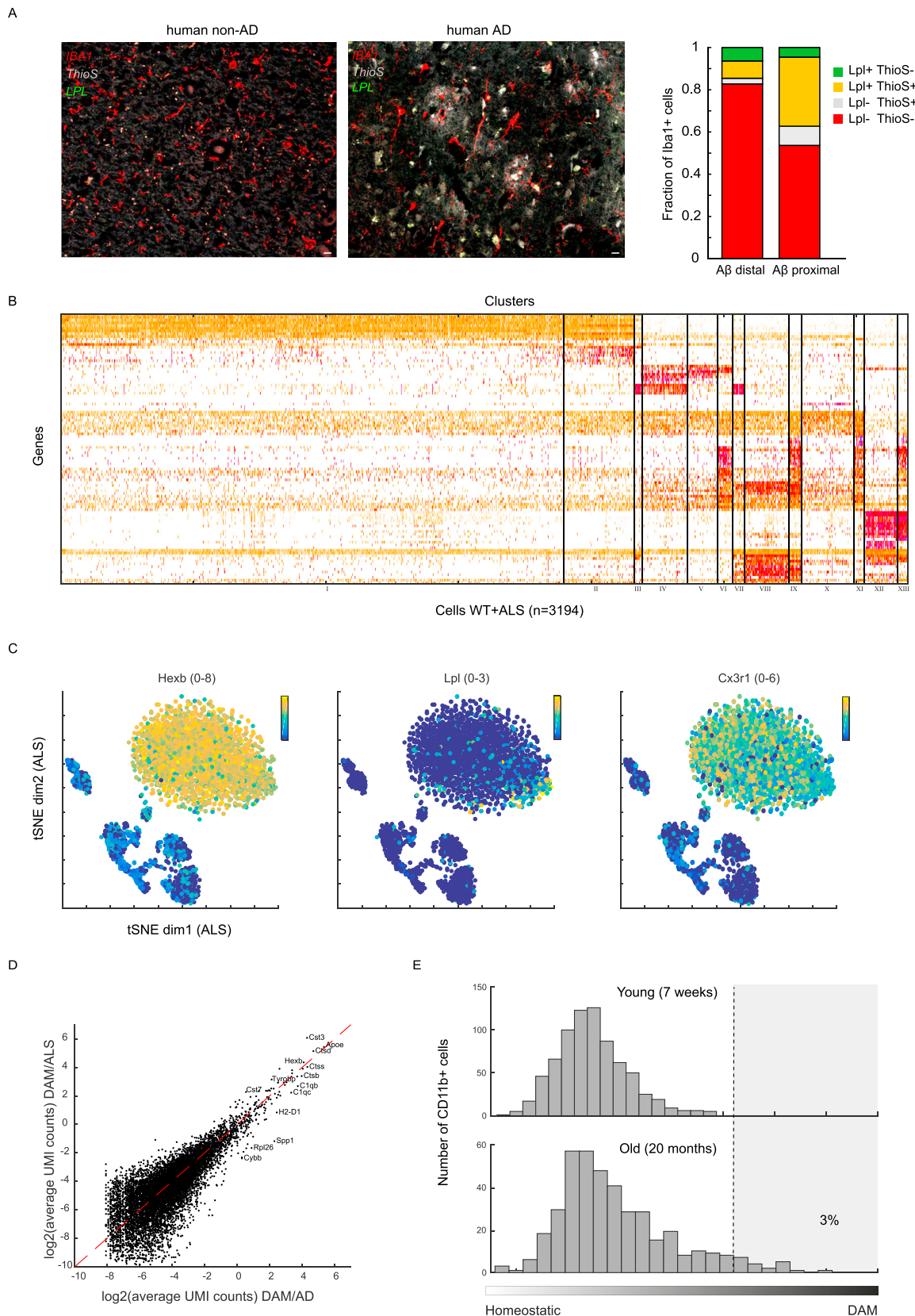
**A****B****C****D**

(legend on next page)

---

**Figure S3. DAM Markers Co-localize in AD Microglia, Related to Figure 3**

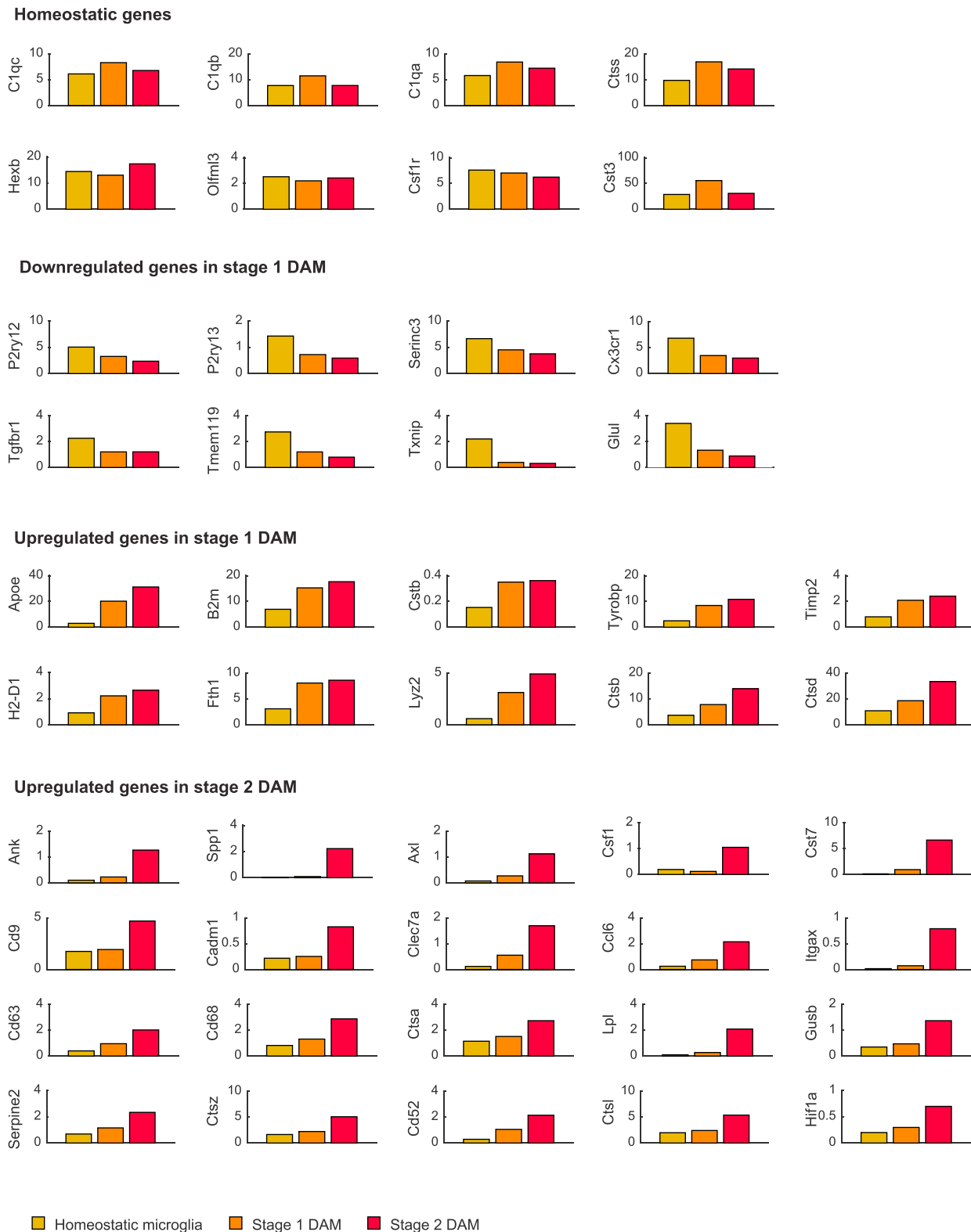
(A) Dot plot quantification for microglia clusters I-X in the cortex/cerebellum experiment, showing the percentage of WT (beige) or AD (red) cells out of the total CD45+ cells in each of the clusters identified in [Figure 3A](#). Each data point (square, male) represents an independent single cell experiment performed on an individual animal. (B) Representative immunofluorescence images of CD11c (green), TIMP2 (cyan) and microglia (IBA-1, red) in cortical sections of 6-month old WT and Tg-AD (AD) mice. Cell nuclei are shown in blue (DAPI). Scale bar, 10  $\mu$ m. Arrows indicate co-localization of TIMP2 and CD11c on IBA-1 positive cells. (C) smFISH of mRNA molecules for Cx3cr1 (green), a marker for homeostatic microglia, and Lpl (red), a DAM marker, together with A $\beta$  plaques immunostaining (gray) and DAPI staining (blue) in intact brain tissue taken from 6-month old WT and AD mice. Imaging of AD mouse brains was performed in a region with low density of A $\beta$  plaques (AD-A $\beta$  distal; bottom left) and in a region with a high density of A $\beta$  plaques (AD-A $\beta$  proximal; right). Large yellow blobs are cytoplasmic auto-fluorescent objects. Scale bar, 5  $\mu$ m. (D) Left - quantification of the number of Lpl molecules in microglia. Horizontal lines are medians, boxes demarcate the 25-75 percentiles; vertical lines are 1.5 times the interquartile range. Red plus signs represent outliers. Right - average UMI count obtained from the single cell RNA-seq data. Quantification was done based on the overall number and size of A $\beta$  plaques in each field. n(WT) = 34, n(AD-A $\beta$  distal) = 38, n(AD-A $\beta$  proximal) = 152, \*\*\* < 0.001. ns = non-significant. Error bars represent SEM.



(legend on next page)

**Figure S4. DAM Are Present in Other Neurodegenerative Conditions in Addition to Alzheimer's, Related to Figure 4**

(A) Representative image of a postmortem AD human hippocampal section ( $n = 5$ ) and a human non-AD brain ( $n = 3$ ) stained for LPL (green), microglia (IBA-1, red) and Thioflavin-S (Thios) for A $\beta$  plaques (gray). Bar plots showing fraction of IBA-1+ cells (microglia) in A $\beta$  distal and proximal regions in postmortem human AD brain ( $n = 110$  cells per region). Shown is a representative quantification of one postmortem brain out of three with a similar pattern. Scale bar, 10  $\mu$ m. (B) Heatmap showing clustering analysis ( $k = 13$ ) of 3194 single cells, featuring 150 most variable genes, from the spinal cord of WT and ALS mouse model. (C) Projection of Hexb, Cx3cr1 and Lpl onto the t-SNE plot depicting the immune cells in an ALS model (corresponding to Figure 4D). The number for each gene represents the max expression level (log<sub>2</sub> UMI counts) depicted by a color bar (similar to Figure 2D). (D) Scatterplot showing the average molecules count (log<sub>2</sub> scale) of DAM in 5XFAD (x axis) compared with DAM in the ALS model (y axis). (E) Bar plots showing the number of microglia cells present in young (7 weeks) and old (20 months) mice along the activation axis. Grey region marks DAM activation area.

**Figure S5. DAM Are Activated through a 2-Step Activation Program, Related to Figure 5**

Bar plots showing mean expression (UMI count) of selected genes across clusters I-III: Homeostatic microglia (yellow), stage 1 DAM (orange) and stage 2 DAM (red).